sustainability

MDPI

Article

Wave Resistance of Floating Offshore Wind Turbines Based on a Viscous-Potential Flow Correction Method: Toward Efficient and Sustainable Wet-Towing Operations

Ning Cui [1], Sheng Yang [1], Chao Tong [2], Xingyu Jiang [2], Rui Ling [2], Mingsheng Chen [2,*] and Yichang Tang [2]

[1] CNOOC Shenzhen Offshore Engineering Solutions Co., Ltd., Shenzhen 518000, China
[2] School of Naval Architecture, Ocean and Energy Power Engineering, Wuhan University of Technology, Wuhan 430063, China
* Correspondence: mschen@whut.edu.cn; Tel.: +86-18271935791

Abstract

Accurate prediction of towing resistance is essential for selecting tug capacity and controlling energy demand during the wet-towing of floating offshore wind turbines (FOWTs). This study established a high-precision CFD numerical wave tank to simulate the towing hydrodynamic performance of the IEA-15 MW semi-submersible FOWT under calm water and regular wave conditions, covering two typical towing layouts (single-column-forward and double-column-forward) and three representative towing speeds. Based on CFD free-decay results, viscous damping corrections in heave, roll, and pitch were applied to the AQWA, while the drag coefficients were introduced through Morison elements. On this basis, an integrated viscous-potential flow coupled numerical model for the tugboat-FOWT system was then established. Frequency-domain analysis showed that wave excitation loads increase with towing speed under following-wave conditions, while the reverse trend occurs under head-wave conditions. Time-domain validation demonstrated that the viscosity-corrected potential flow model achieves a deviation below 2% for calm water resistance and less than 5% for mean wave resistance compared with high-fidelity CFD benchmarks. Parametric analysis under multiple regular wave conditions revealed that wave-added resistance first increases and then falls as wave period increases, consistent with the variation in surge wave excitation forces, and exhibits a nonlinear growth pattern with wave height. The double-column forward layout yields overall higher towing resistance than its single-column alternative, while main towline tension can accurately reflect the total towing resistance level. These technical outcomes provide actionable engineering guidance for low-carbon, cost-effective wet-towing scheme formulation, facilitating the sustainable, large-scale exploitation of deep-sea wind resources and advancing the long-term decarbonization of the marine energy sector.

Keywords: semi-submersible platform; hydrodynamic correction; encounter frequency; towline load; operational efficiency

Check for updates

Academic Editors: Tiago Fazeres Ferradosa, Mario López Gallego, Paulo Jorge Rosa-Santos, Dawei Guan and Daniel Clemente

Received: 31 July 2026
Revised: 14 September 2026
Accepted: 16 September 2026
Published: 23 September 2026

Copyright: © 2026 by the authors. Licensee MDPI, Basel, Switzerland. This article is an open access article distributed under the terms and conditions of the Creative Commons Attribution (CC BY) license.

1. Introduction

Global warming and the gradual depletion of traditional energy sources such as oil and natural gas are driving the transition toward a green and low-carbon energy structure. Clean and renewable energy is gaining increasing attention, and its development is accelerating. Against this backdrop, marine renewable energy has attracted widespread interest worldwide [1]. In a broad sense, marine renewable energy includes tidal current

energy, wave energy, ocean thermal energy, solar energy, and wind energy [2]. Among these, offshore wind energy represents a significant form of marine renewable energy. In China, the wind energy potential in waters shallower than 50 m is approximately 700 million kW, while the total wind energy resource in deep and distant waters reaches about 1.3 billion kW [3]. Compared to onshore wind resources, offshore wind resources are generally more stable, which benefits power generation efficiency and output stability. Deep and distant seas possess richer wind energy resources than near-shore areas. In recent years, the development and utilization of near-shore wind resources has become increasingly saturated [4]. Therefore, harnessing deep-sea wind energy is an inevitable trend for future marine economic development.

Offshore wind farms are key facilities for capturing marine wind energy, and offshore wind technology has become a research hotspot both domestically and internationally [5]. As offshore wind farms move toward deep and distant waters, fixed foundations commonly used in near-shore areas become unsuitable for deep-water environments. Floating offshore wind turbines (FOWTs) offer a promising option for harvesting deep-sea wind energy. Although FOWTs have advantages in deep waters, economic and safety concerns still constrain their development [6]. In the cost of projects such as "Sanxia Linghang" and "Fuyao," installation costs account for more than 20% of the total. In 2023, offshore wind safety accidents during the installation phase accounted for 62% of the annual total. "How to overcome key technology R&D and engineering demonstration challenges for floating offshore wind?" was listed among the top ten industrial technology problems released by Chinese scientific research institutions in 2021. Reducing installation costs and improving construction safety are of great significance for the development of floating wind power. Transportation and installation account for a large proportion of the entire FOWT installation phase. These operations feature long durations and extensive travel distances. Therefore, ensuring transportation safety and shortening the transportation cycle are critical for cost reduction and efficiency improvement during the installation phase. In this context, research on the transportation and installation phase of FOWTs is of great significance. It helps optimize transportation and installation schemes, evaluate operational safety, and predict weather windows. This contributes to cost reduction and efficiency improvement during transportation and installation, promotes the development and utilization of deep-sea resources, and strengthens the scale of China's marine economy.

The construction and installation of FOWTs typically involves several stages: floating foundation construction, foundation transportation, turbine assembly at the quayside, integrated wet-towing of the FOWT, and in-place mooring installation [6]. Among these, the transportation and installation phase lasts for a relatively long duration, which involves the transportation of both the foundation and the integrated FOWT. Among existing FOWT transportation methods, wet-towing is widely used. For instance, the WindFloat Atlantic project in Portugal employed wet-towing for its floating turbines. The Floatgen project in France also used wet-towing to transport a 2 MW prototype. The Fukushima Mirai project in Japan and the Kincardine project in the UK similarly adopted wet-towing. Domestically, all five Chinese floating wind turbine projects used wet-towing for transportation. In 2021, China's first floating wind turbine test prototype "Sanxia Linghang" was successfully towed by the Guangzhou Salvage Bureau's tugboat "Dehui" to the Yangjiang sea area, 16 nautical miles off the coast. In 2022, China's first deep-sea floating wind power equipment "Fuyao" was towed by the Nanhai Rescue Bureau's vessel "Nanhai Jiu 101" from the Maoming port in Guangdong. After a long tow of 110 nautical miles, it reached the Luodousha sea area in Zhanjiang, Guangdong, with an average water depth of 65 m. In 2023, China's first deep-sea floating wind power platform "Haiyou Guanlan" was towed by the Shanghai Salvage Bureau's vessel "Huahu" from the Zhuhai shipyard. After approximately 180 nautical

miles, it arrived at the Wenchang sea area in Hainan. In the same year, the world's first floating wind-fishery integration project "Guoneng Gongxiang" was successfully launched and towed to its designated target. In 2024, the world's largest single-capacity floating wind power platform "Mingyang Tiancheng" departed from Guangzhou Nansha port. Towed by Zhengli Offshore Engineering's vessel "Zhengli 18,000," it embarked on its journey to the Mingyang Qingzhou IV offshore wind farm in Yangjiang, Guangdong. The total voyage was 191 nautical miles and lasted over 50 h.

Recent research on FOWT wet-towing has advanced from global motion assessment toward direct evaluation of towing resistance and operational planning. Researchers have employed potential flow formulations [7–10], hybrid models that combine potential flow theory with Morison's equation, towing tank experiments [4,6,11–13], CFD analyses [14,15], ship simulator studies [16], and fully coupled numerical models [17–20] to examine platform motions, towline loads, towing resistance, heading control, and operational feasibility. Collectively, these studies provide a sound basis for evaluating towing responses and operational safety. Nevertheless, most numerical approaches remain specific to individual platforms and require separate simulations whenever the towing speed, draft, wave conditions, or towing configuration changes. This limitation restricts their suitability for rapid towing system design and preliminary operational assessment.

The transportation and installation of FOWTs involves long durations, extensive distances, and complex marine environments. Scholars worldwide have conducted extensive research on FOWT motion characteristics, environmental load effects, and towline properties during the transportation and installation phase. Ramachandran et al. [4] performed hydrodynamic analyses of a 5 MW FOWT foundation under towing conditions and validated the numerical results through experiments. Subsequently, Ramachandran et al. [4] conducted experimental studies on the OC4 floating wind turbine platform. They established a numerical model combining potential flow theory with Morison's equation, analyzed the towing motion performance of the OC4 platform, and found that the hybrid method yielded good results for all towing speeds and wave heights. Le et al. [13] proposed a submersible tension-leg wind turbine (STPLWT) suitable for wet-towing. They established a towing system numerical model including the tugboat, towline, and wind turbine, and investigated towing stability and the effect of tow point height on the towing system. Le et al. [13] established a towing system numerical model for a novel 10 MW fully submerged floating wind turbine concept (SFOWT). They validated the numerical model against experiments and then used numerical simulations to analyze the towing performance of three-column and four-column SFOWTs under different wave conditions. They found that both configurations exhibited good towing performance under permissible conditions. Yin et al. [6] conducted towing experiments based on the INO WINDMOOR semi-submersible wind turbine platform, examining towing resistance and dynamic response. Pivert et al. [19] proposed a method for optimizing offshore FOWT towing routes. This method used a dedicated vessel simulator to generate datasets describing towing arrangement dynamics and engine data. Using this dataset and historical meteorological data, multi-objective path optimization was performed with objectives of minimizing towing duration, maximum towline tension, and carbon emissions. Chen et al. [7] used STAR-CCM+ to analyze the calm water towing resistance of a 5 MW FOWT. They then established a towing system numerical model in ANSYS-AQWA including the FOWT, towline, and tugboat and studied the motion response during the entire towing process through flow coefficient simulations. Lian et al. [20] proposed a novel integrated prefabrication and transportation technology based on bucket foundations. They introduced the concept of U-K barge semi-wet-towing and conducted a series of experiments to validate the feasibility of the scheme. Tang et al. [10] established an integrated towing system numerical model

of a fully submerged FOWT-towline-tugboat using the Moses software. They studied the effects of wind speed and wave direction on the towing motion response of fully submerged FOWTs, finding that larger wind speeds led to greater turbine motion amplitudes. Wang et al. [21] used ANSYS-AQWA to study the effect of heave plate size and shape on platform motion for floating wind turbine platforms. They found that heave plate shape had no significant effect on the hydrodynamic performance of the foundation and that an optimal heave plate size exists for semi-submersible wind turbine foundations. In terms of the numerical simulation of the towing process under different thrust control strategies, Wang et al. (2026) [22] further discussed the hydrodynamic differences of navigation bodies under constant-speed towing and fixed-thrust towing constraints.

Towing resistance prediction is a core technical aspect of marine floating structure transportation and installation operations. Its accuracy is crucial for engineering safety and economic optimization, especially when the floating wind turbine operates in shallow water areas with obvious additional resistance effects caused by water depth limitation [23]. As wind turbines scale up, floating foundation dimensions increase accordingly, leading to higher towing resistance. For example, the 5 MW OC4 platform has a calm water towing resistance of approximately 120 tons at 4 knots [4], while the INO WINDMOOR 12 MW platform reaches over 150 tons at the same speed [6]. Additionally, according to DNV requirements, tugboat power derating must be considered. Thus, for future 15 MW or even 20 MW+ FOWT towing operations, considering tugboat power derating and wave effects, towing force requirements may exceed 200 tons. This places higher demands on tugboats, yet tugboat resources face severe challenges, particularly for large tugboats. As FOWT unit capacity continues to increase, the overall size and towing resistance of FOWTs keep growing. Future large-megawatt FOWT towing operations may require towing forces exceeding the 200-ton level. Combined with the inherent power derating of tugboat main engines during navigation, the demand for professional large tugboats with ultra-high bollard pull is becoming increasingly urgent. A review of major large tugboats with bollard pull exceeding 200 tons worldwide shows that, domestically, vessels with strong towing capability are mainly concentrated in the Guangzhou Salvage Bureau, Shanghai Salvage Bureau, Nanhai Rescue Bureau, CNOOC Services, Offshore Oil Engineering, and Zhengli Offshore Engineering. Among these, vessels such as Nanhai Jiu 103, Haiyang Shiyou 291, and Island Victory stand out in towing performance. Some vessels are equipped with DP dynamic positioning systems, which can further enhance towing operation stability. However, overall, the domestic inventory of high-specification large tugboats suitable for long-distance wet-towing of deep-sea FOWTs is limited. Tugboat selection, allocation, and capacity coordination face considerable difficulties. Therefore, accurate towing resistance prediction is of great significance for tugboat selection, resource allocation, and towing safety assurance.

Scholars worldwide have conducted extensive research on FOWT towing performance. For towing resistance prediction, computational fluid dynamics (CFD) numerical simulation, experimental research, and empirical methods are mainly used. For instance, Hmedi et al. [24] used experiments to study the resistance differences of the CENTEC-TLP platform in calm water and wave environments. Ramachandran et al. [4] used empirical load formulas from the offshore industry to calculate current forces, quantitatively analyzing the effects of different flow velocities on the overall motion response and stability of FOWT towing systems. To achieve faster and more accurate towing resistance prediction, scholars have made considerable efforts, extending beyond FOWT resistance studies to include other marine floating structures. Zhang et al. [15] combined tank model tests with CFD numerical simulation to investigate the hydrodynamic towing resistance and flow field evolution characteristics of composite bucket foundations. Comparing results with and

without internal compartment structures, they found that the total towing resistance of compartmented bucket foundations was significantly lower than that of non-compartmented configurations. Yousefifard et al. [25] conducted numerical simulations of towing resistance for a novel hourglass-shaped FPSO under multiple draft conditions, accounting for additional resistance effects from free surface sloshing in tanks. Their study showed that the total resistance of this unconventional floating body was dominated by pressure drag, with viscous friction resistance accounting for a much smaller proportion than in conventional FPSO hull forms. Qu et al. [26] conducted calm water towing model tests and CFD turbulent flow simulations for a self-propelled jack-up offshore platform. Their results showed that flow blockage and flow separation readily formed at the platform bow, with viscous pressure drag dominating the total towing resistance.

CFD methods deliver high prediction precision but suffer from prohibitive computational costs, which raise the carbon footprint of numerical simulation workflows and cannot support large-scale parametric optimization for sustainable towing design. Conventional pure potential flow algorithms drastically underestimate viscous dissipation, leading to biased towing resistance results and overly conservative tug allocation schemes. To address this defect, viscous correction modifications for potential flow theory have been continuously developed and applied in the hydrodynamic analysis of floating wind turbines and multi-body floating coupling systems in recent years [27–29]. To balance calculation efficiency and prediction accuracy while providing a low-carbon numerical tool for sustainable FOWT wet-towing design, this study novelly establishes a viscous-potential flow coupled correction framework. The core research workflow is structured as follows:

(a) Construct high-fidelity CFD numerical wave tanks to precisely calculate wave-induced towing resistance of the IEA-15 MW semi-submersible FOWT under variable wave heights, periods and towing layouts;
(b) Calibrate viscous damping coefficients via CFD free-decay motion data, and embed Morison-element drag corrections into ANSYS-AQWA potential flow modules to establish a tug–FOWT integrated coupled numerical model;
(c) Systematically quantify the influence laws of towing velocity, structural layout, wave period and wave height on wave-added resistance, and generate quantitative technical guidance for cost-efficient wet-towing scheme optimization.

Beyond its engineering significance, accurate towing-resistance prediction is, in essence, a sustainability issue for the offshore wind sector. A wet-tow of a 15 MW-class FOWT over typical distances of 110–180 nautical miles requires one or more large seagoing tugs running continuously. An over-conservative resistance estimate compels overpowered tug chartering and unnecessarily wide weather margins, inflating fuel consumption, exhaust emissions, and cost, whereas under-prediction jeopardizes towing safety. The present study therefore addresses the environmental (fuel and emissions), economic (installation cost and LCOE), and safety dimensions of sustainable development simultaneously, in line with Sustainable Development Goals (SDGs) 7, 9, and 13.

The remainder of this article is organized as follows. Section 2 presents the governing equations, platform and tugboat models, CFD configuration, numerical verification, viscous correction procedure, and coupled towing system. Section 3 reports the CFD and corrected potential flow results, including wave quality, flow field characteristics, frequency domain loads, time domain verification, towing resistance, towline tension, and wave parameter effects. Section 4 discusses model accuracy, physical mechanisms, towing layout selection, methodological recommendations, sustainability implications, assumptions, and limitations. Section 5 summarizes the principal quantitative findings and defines the conditions under which the method can be applied.

2. Materials and Methods

2.1. RANS Equations and Turbulence Model

In practical engineering applications, fluid flow is mostly turbulent and unsteady. For such flows, the Reynolds-averaged Navier–Stokes (RANS) equations are used as the governing equations to solve the flow field [30]. These equations are derived by time-averaging (or Reynolds-averaging) the Navier–Stokes (NS) equations. Equation (1) represents the continuity equation (mass conservation), and Equation (2) represents the momentum conservation equation [31]:

$$\frac{\partial(\rho u_i)}{\partial x_i} = 0, \tag{1}$$

$$\frac{\partial}{\partial t}(\rho u_i) + \frac{\partial}{\partial x_i}(\rho u_i u_j) = -\frac{\partial p}{\partial x_i} + \frac{\partial}{\partial x_i}\left(\mu\frac{\partial u_i}{\partial x_j} - \rho\overline{uu_j'} + \rho S_i\right), \tag{2}$$

where u_i and u_j are the velocity vector components in the x_i and x_j directions; p is pressure; $-\rho\overline{uu_j'}$ is the Reynolds stress component; and S_i is the body force.

The RANS equations decompose instantaneous quantities in turbulent flow fields into mean values and fluctuating components [32]. For example, the velocity component is decomposed as $u_i = \overline{u_i} + u_i'$. Substituting this into the NS equations and time-averaging yields the conservation equations satisfied by the mean quantities. Reynolds stress terms (such as $-\rho\overline{uu_j'}$) appear in these equations, reflecting the effect of turbulent fluctuations on the mean flow. These terms must be closed through turbulence models [33]. The *k*-*ε* model is one of the most widely used models in industry. It includes the standard *k*-*ε* model and the realizable *k*-*ε* model, both suitable for high-Reynolds-number turbulence. For floating platform structures, the characteristic length is large, and the towing speed is relatively high. The fluid flow encountered during navigation is basically high-Reynolds-number flow, with Reynolds numbers reaching millions or tens of millions [34]. This study uses the realizable *k*-*ε* model, which has moderate computational cost and only requires solving two transport equations for turbulent kinetic energy k and turbulent dissipation rate ε. The transport equations for turbulent kinetic energy k and turbulent dissipation rate ε are:

$$\frac{\partial}{\partial t}(\rho k) + \nabla\cdot(\rho k\overline{v}) = \nabla\cdot\left[\left(\mu + \frac{\mu_t}{\sigma_k}\right)\nabla k\right] + P_k - \rho(\varepsilon - \varepsilon_0) + S_k, \tag{3}$$

$$\frac{\partial}{\partial t}(\rho\varepsilon) + \nabla\cdot(\rho\varepsilon\overline{v}) = \nabla\cdot\left[\left(\mu + \frac{\mu_t}{\sigma_\varepsilon}\right)\nabla\varepsilon\right] + \frac{1}{T_e}C_{\varepsilon1}P_\varepsilon - C_{\varepsilon2}f_2\rho\left(\frac{\varepsilon}{T_e} - \frac{\varepsilon_0}{T_0}\right) + S_\varepsilon, \tag{4}$$

where $\overline{v}$ is the mean velocity; σ_k, σ_ε, $C_{\varepsilon1}$, and $C_{\varepsilon2}$ are model coefficients; P_k and P_ε are production terms; f_2 is the damping function; and S_k and S_ε are user-defined source terms.

For near-wall treatment, the *k*-*ε* model provides a two-layer all-y+ method. This method is applicable to high-Reynolds-number grids (y+ > 30) and also works well for low-Reynolds-number grids (y+ < 1).

The near-wall dissipation rate for the two-layer model can be simply expressed as:

$$\varepsilon = \frac{k^{3/2}}{l_\varepsilon}, \tag{5}$$

where l_ε is the length scale function.

2.2. Potential Flow and Floating Body Dynamics

Potential flow theory is a fundamental fluid mechanics theory based on the assumptions of inviscid, irrotational, and incompressible flow [35]. It provides a simplified de-

scription of ideal fluid flow problems. By introducing the velocity potential function, fluid velocity is expressed as the gradient of the potential function. The flow field governing equations are then reduced to the Laplace equation [36], enabling a linear description of fluid motion. As a classical tool for studying the interaction between offshore structures and waves, potential flow theory offers advantages of high computational efficiency, simple mathematical form, and strong analytical capability [37].

The velocity potential function can be defined as:

$$\phi(x,y,z,t) = \mathrm{Re}\left\{\hat{\phi}(x,y,z,t)e^{i\omega t}\right\}, \tag{6}$$

where the superscript ˆ denotes complex amplitude; w is the wave frequency; x is the spatial coordinate of any point in the flow field; and t is time.

The Laplace equation is:

$$\nabla^2\hat{\phi}(x,y,z,t) = 0, \tag{7}$$

2.3. Platform Geometry and CFD Model

The frequency-domain motion equations in ANSYS-AQWA 2025R1 are based on linear potential flow theory and floating body six-degree-of-freedom dynamics [38]. The coupling effect between floating body motion and radiated waves is described through added mass and radiation damping matrices [39]. Hydrostatic restoring force and system-added stiffness together constitute the restoring force term, and external excitation forces consist of wave excitation forces and drag forces [38]:

$$\left(M + A_{ij}\right)\ddot{x}_{0j} + \left[B_{ij}(U_0) + B_v\right]\dot{x}_{0j} + C_{ij}x_{0j} = F_E + F_{drag}, \tag{8}$$

where M is mass; A_{ij} is added mass; B_{ij} is the radiation damping coefficient with forward speed; B_v is viscous damping; C_{ij} is hydrostatic restoring stiffness; U_0 is towing speed; F_E is wave excitation force; and F_{drag} is drag force, which can be added through Morison elements.

AQWA's time-domain solution is based on linear potential flow radiation–diffraction theory. Frequency-domain hydrodynamic coefficients are transformed into time-domain kernel functions, yielding the time-domain convolution equation for floating body six-degree-of-freedom motion, known as the Cummins equation. During towing, the towing system is subjected to external loads from wind, waves, current, and towlines. The time-domain motion equation of the floating wind turbine can be described as [40]:

$$\begin{aligned}\left[M + A_{ij}(\infty)\right]\ddot{x}_{0j}(t) + B_v\dot{x}_{0j}(t) + \int_0^t K(t-\tau)\dot{x}_{0j}(\tau)d\tau + C_{ij}x_{0j}(t)\\ = F_{exc}(t) + F_{cable}(t) + F_{others}(t),\end{aligned} \tag{9}$$

where $A_{ij}(\infty)$ is the added mass at infinite wave frequency; $K(t)$ is the impulse response function; $F_{exc}(t)$ is wave excitation load; $F_{cable}(t)$ is towline load; and $F_{others}(t)$ represents other loads.

3. Numerical Model Construction

3.1. FOWT Computational Model Establishment

A numerical model for calculating the towing resistance of the IEA-15MW floating wind turbine in waves was established in STAR-CCM+. In this study, the wind resistance is negligible compared to flow resistance at low wind speeds. Therefore, the upper wind turbine was not modeled when establishing the numerical model for towing resistance in waves. Due to the structural symmetry of the FOWT, a half-model and computational domain were used to reduce overall unknowns. The configuration of the computational

model is shown in Figure 1. When calculating the towing resistance of the FOWT in waves, the DFBI (Dynamic Fluid Body Interaction) and overset mesh techniques were used to account for turbine motion. The red region in the figure represents the motion zone, and the remaining region represents the overall fluid computational domain. The computational domain size and boundary settings are consistent with those used for calm water towing resistance calculations. However, a wave damping method was used to suppress wave reflection, with the damping zone set to 1.5 times the wavelength. The structure retains two degrees of freedom, heave and pitch, and the towing speed was simulated by applying forward speed to the waves.

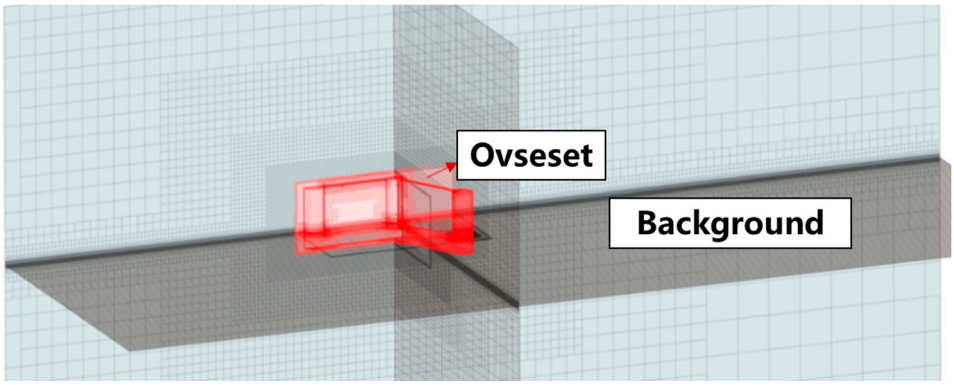

Figure 1. Numerical model for FOWT wave resistance calculation.

The properties of the floating wind turbine are listed in Table 1, where the parameters were obtained through SOLIDWORKS modeling and exported property data.

Table 1. Properties of the floating wind turbine.

Parameters	IEA-15MW Floating Wind Turbine
Center of gravity coordinates (m)	(0, 0, 10.985)
Draft (m)	10
Design displacement (m^3)	15,739.4
I_{xx} ($kg \cdot m^2$)	3.972×10^{10}
I_{yy} ($kg \cdot m^2$)	3.962×10^{10}
I_{zz} ($kg \cdot m^2$)	1.997×10^{10}

3.2. Mesh Generation and Verification

The mesh discretization scheme adopted for the computational domain remains largely consistent with the setup for calm water towing resistance simulations. By contrast, wave resistance computations require dedicated wave generation settings, where high-fidelity wave propagation and accurate wave–structure interaction must be guaranteed. Accordingly, extra mesh refinement is performed on the free-surface region. Alsubal et al. [41] discussed the performance of numerical wave generation using STAR-CCM+ and proposed mesh division criteria: at least 100 cells per wavelength in the wave propagation direction, at least 20 cells per wave height in the vertical direction, and an aspect ratio less than 10. They also noted that the time step should satisfy $\Delta t \leq T/100$.

3.3. Results and Analysis

3.3.1. Wave Time Histories at Different Towing Speeds

CFD calculations were performed for both single-column-forward and double-column-forward towing at 2, 3, and 4 knots, under regular head-on waves with a wave height of 2.0 m and a period of 6 s. Forward speed was applied to the waves to simulate the

FOWT towing speed. A wave monitoring point was set at one wavelength ahead of the FOWT. Figure 2 shows the wave time histories at different towing speeds over six natural periods T_0. Due to the speed effect, the wave encounter period is smaller than the natural period of 6 s. At 2, 3, and 4 knots, the encounter periods are 5.406 s, 5.151 s, and 4.919 s, respectively. As towing speed increases, more waves are encountered in the same time period. Comparison of simulated wave height and period with theoretical values shows that the relative error in wave height is less than 5%, and the period matches well with the theoretical value, indicating good wave quality.

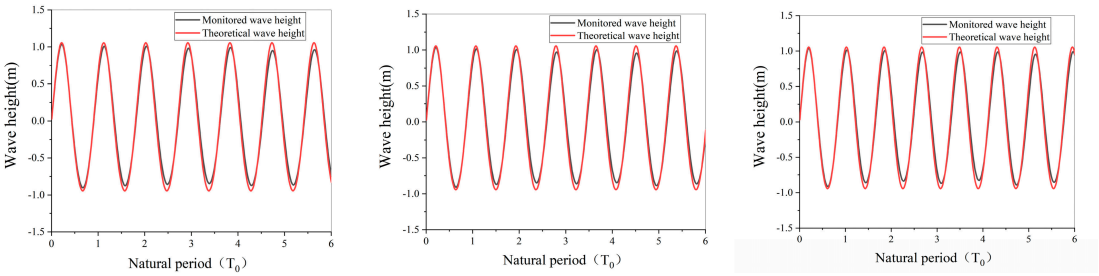

Figure 2. Wave time histories at different towing speeds: (**a**) 2 kn; (**b**) 3 kn; (**c**) 4 kn.

The towing speeds of 2, 3, and 4 kn represent low, intermediate, and upper operating conditions for the modeled single tug system. At 4 kn, the calm water resistance already exceeds 1.6 MN for the single column forward arrangement and 2.1 MN for the double column forward arrangement. The corresponding bollard pull requirement becomes critical after tug power derating is applied. Speeds above 4 kn were therefore excluded from the present validation range. Extension to 5 or 6 kn may be technically possible with a higher capacity tug or a multiple tug arrangement, but it requires new checks of towline strength, dynamic load amplification, hydrodynamic coefficients, and operational limits. The present results should not be extrapolated beyond 4 kn without additional calibration.

3.3.2. Comparison of Mean Wave Resistance

Resistance calculations for the FOWT were performed, and the results are shown in Figure 3. In regular waves, the towing resistance increases with increasing towing speed. For single-column-forward towing, the mean towing resistances at 2, 3, and 4 knots are 505.73 kn, 1039.18 kn, and 1670.55 kn, respectively. For double-column-forward towing, the mean towing resistances are 621.04 kn, 1289.51 kn, and 2311.35 kn, respectively. In the wave towing conditions, double-column-forward towing shows relatively high resistance than single-column-forward towing.

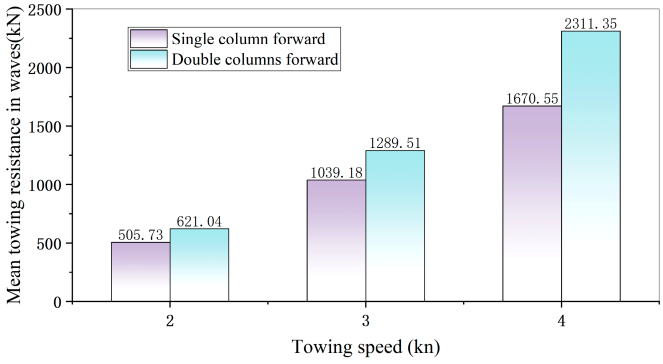

Figure 3. Mean wave resistance for single/double-column-forward conditions at different towing speeds.

3.3.3. Flow Field Velocity Distribution

Figure 4 shows the free surface velocity contours of the FOWT at different towing speeds and configurations. For double-column-forward towing, the two columns face the incoming waves together, forming a broader high-velocity region on the wave-facing side. Wave diffraction introduces stronger wave interactions between the columns. For single-column-forward towing, the wave-facing side is directly exposed to waves through a single column. Since the side columns are positioned aft, their influence on the wave-facing region is smaller, resulting in a narrower velocity distribution compared to double-column-forward towing. As towing speed increases from 2 to 4 knots, the wake region increases for both configurations, and the wake trajectory becomes more pronounced.

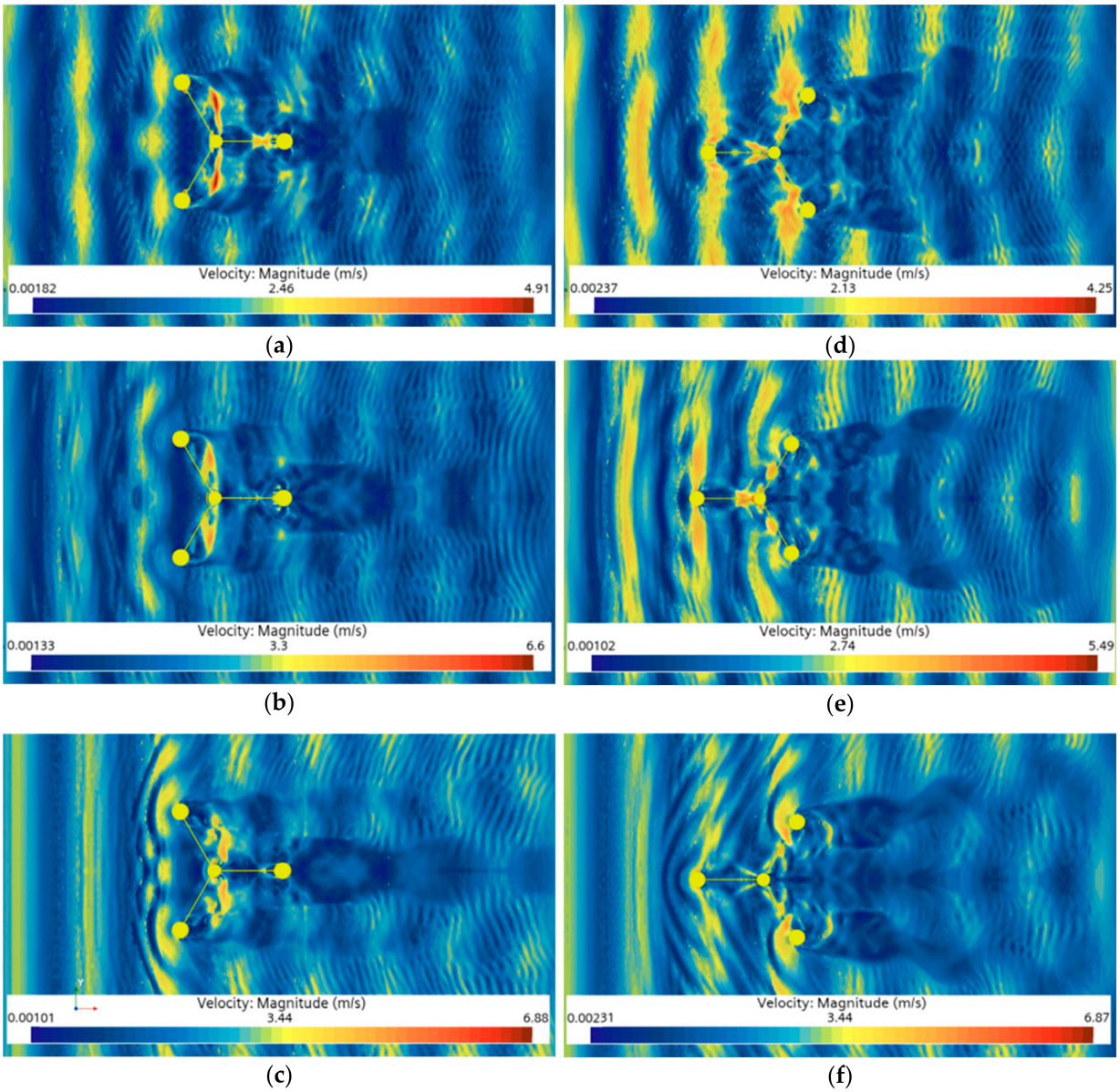

Figure 4. Free surface velocity contours of FOWT towing: (**a**) double-column-forward (2 kn); (**b**) double-column-forward (3 kn); (**c**) double-column-forward (4 kn); (**d**) single-column-forward (2 kn); (**e**) single-column-forward (3 kn); (**f**) single-column-forward (4 kn).

4. Viscous-Potential-Flow-Corrected Towing Calculations

4.1. AQWA Numerical Model Setup

Potential flow methods were used to analyze the towing resistance characteristics of the FOWT. A towing system model for the FOWT was established in ANSYS-AQWA, as shown in Figure 5. Here, towing speed was simulated by adding an equivalent flow velocity. The tugboat was restricted in the X-direction to prevent system drift. For double-column-forward towing, the tugboat and FOWT are connected through a triangle plate and towlines, with a 60° angle between the towlines. For single-column-forward towing, a direct main towline connection is used. The model can be built using nested Morison elements within Panel elements to correct for the viscous effects neglected by potential flow theory. Morison elements are scaled and drag coefficients are added based on CFD results to calculate towing resistance.



Figure 5. FOWT towing system model in AQWA: (**a**) towing system model; (**b**) FOWT model.

Calm water towing resistance as a function of towing speed was calculated by CFD, as shown in Figure 6. The calm water resistance of the FOWT at 4 knots already exceeds 1600 kn. According to DNV requirements, a minimum tugboat power derating of 20% must be considered. This indicates that the tugboat bollard pull must be at least at the 200-ton level. Therefore, the tugboat "Deqiang" from the Guangzhou Salvage Bureau was used as the prototype in this study, and the geometric parameters of the tugboat are listed in Table 2.

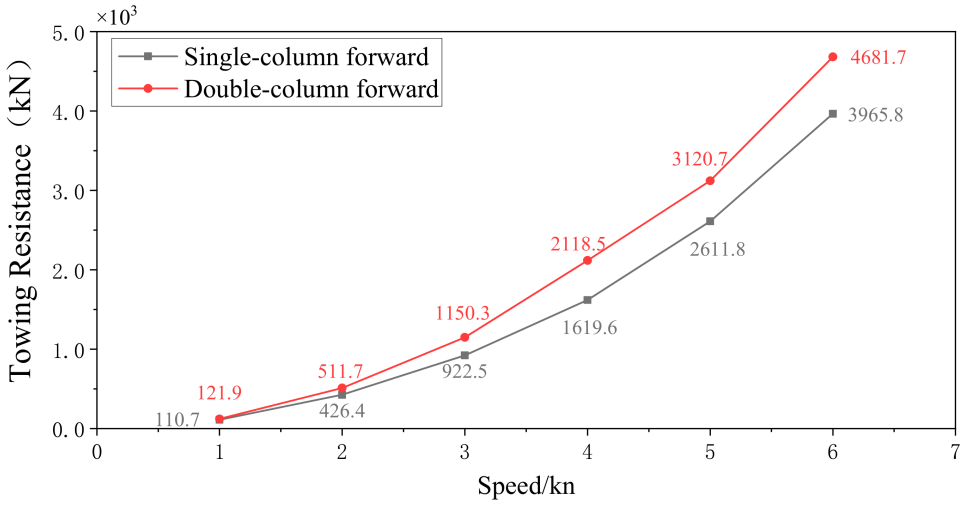

Figure 6. Calm water towing resistance.

Table 2. Tugboat parameters.

Parameters	Deqiang Tugboat
Center of gravity coordinates (m)	(0, 0, 0)
Draft (m)	7.2
Design displacement (m^3)	4817.5
I_{xx} ($kg \cdot m^2$)	1.572×10^8
I_{yy} ($kg \cdot m^2$)	1.694×10^9
I_{zz} ($kg \cdot m^2$)	1.832×10^9

4.2. Viscous Damping and Drag Coefficient Correction Based on CFD Results

ANSYS-AQWA performs hydrodynamic calculations based on potential flow theory. This theory assumes an inviscid fluid and neglects viscous effects, thus failing to account for viscous energy dissipation. However, in practical engineering applications, viscous effects significantly influence floating body motion amplitude and load levels, particularly for low-damping degrees of freedom such as heave, roll, and pitch. Therefore, to more accurately simulate the dynamic response of the FOWT towing system, damping corrections must be applied to account for fluid viscosity and compensate for the damping effect of viscous energy dissipation on system response.

CFD methods were used to calculate the free decay motion of the FOWT, providing decay data in the heave, roll, and pitch directions for damping correction. For N decay cycles, the logarithmic decrement and damping ratio are calculated as:

$$\begin{aligned} \delta &= \frac{1}{N}\ln\left(\frac{X_1}{X_{N+1}}\right), \\ \zeta &= \frac{\delta}{\sqrt{4\pi^2+\delta^2}} \end{aligned} \tag{10}$$

and the corresponding equivalent linear damping is:

$$B_{eq} = 2\zeta\sqrt{(M + A_{33})C_{33}} \tag{11}$$

Because radiation damping is already included in AQWA, the supplementary viscous term is selected so that the total linear damping at the relevant natural frequency agrees with the CFD-derived value.

$$\zeta \approx \frac{1}{2\pi N}\ln\left(\frac{X_1}{X_{N+1}}\right) \tag{12}$$

is the small damping approximation of the exact logarithmic decrement relation. For the identified damping ratios of 4.2–5.0%, the difference between the exact and approximate relations is only 0.09–0.13% relative to the damping ratio. The CFD-derived correction coefficients and the corresponding decay comparisons are shown in Figure 7; the corrected floating body motion decay curves agree well with the CFD results. The tugboat damping correction was performed using the same method in the further research.

The agreement between the corrected potential flow model and CFD demonstrates numerical consistency across two formulations, but it does not constitute independent experimental validation. Experimental measurements for the same IEA 15 MW platform, draft, towing layout, speed range, and wave conditions are not available in the present study. The reported error levels should therefore be interpreted as deviations from the CFD benchmark.

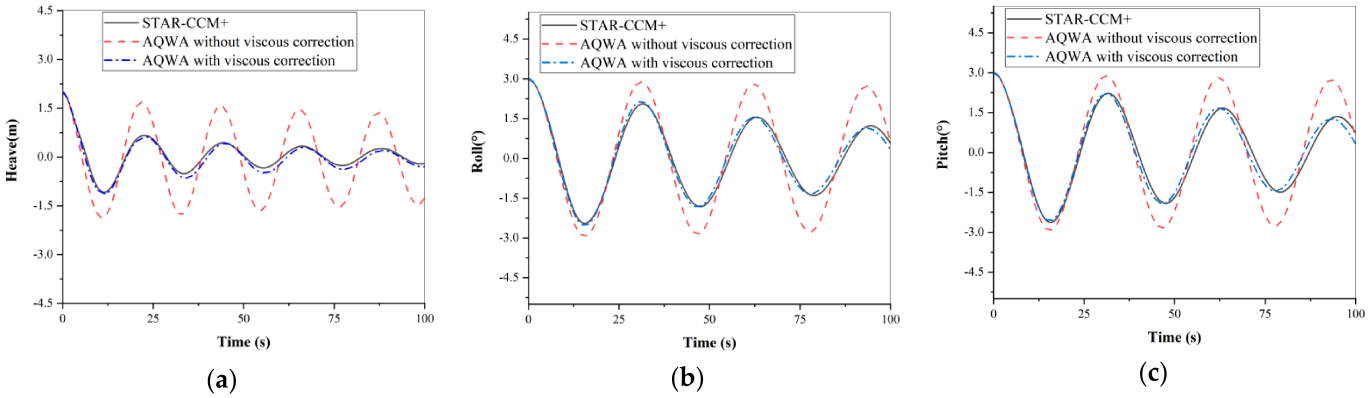

Figure 7. Free decay curves: (**a**) heave decay; (**b**) roll decay; (**c**) pitch decay.

4.3. Frequency-Domain Hydrodynamic Analysis

4.3.1. Load Patterns for Double-Column-Forward Configuration

Hydrodynamic performance of the tugboat–FOWT coupled system under various towing speeds and layouts was analyzed. Wave excitation loads acting on the floating platform were further compared at towing speeds of 2, 3 and 4 knots to clarify the speed-dependent hydrodynamic influences. Figure 8 presents the wave excitation loads of the double-column-forward configuration across all tested speeds. For incident wave angles ranging from 0° to 45°, wave excitation loads rise as towing speed increases; the reverse tendency appears for wave directions of 135–180°. Such variation rules hold true for all three degrees of freedom. In general, towing speed amplifies the wave excitation responses when the FOWT travels under following seas. The speed-induced discrepancies are more prominent for low-frequency waves below 1.0 rad/s and gradually diminish with increasing wave frequency, with this phenomenon being more distinct under following-wave conditions.

4.3.2. Load Patterns for Single-Column-Forward Configuration

Figure 9 shows the wave excitation loads on the FOWT at different towing speeds for single-column-forward towing. Similar to double-column-forward towing, wave excitation loads increase with towing speed in the following-wave direction and decrease in the head-wave direction. However, different towing configurations also exhibit distinct characteristics. This is mainly reflected in the heave direction, where single-column-forward towing is more sensitive to following waves. The wave excitation load in the 0° direction is significantly larger than that in other directions and also larger than the load for double-column-forward towing, while double-column-forward towing shows higher sensitivity to oblique waves.

4.4. Time-Domain Validation

Before conducting time-domain dynamic response calculations, it is necessary to perform consistency checks on the motion characteristics of multiple degrees of freedom of the FOWT towing system under free-floating conditions. Specifically, motion response results obtained from frequency-domain RAOs are compared with those from time-domain solutions. This verifies the consistency of the time-domain model with frequency-domain predictions in terms of motion amplitude, phase, and main response patterns, ensuring the reliability and accuracy of subsequent time-domain results.

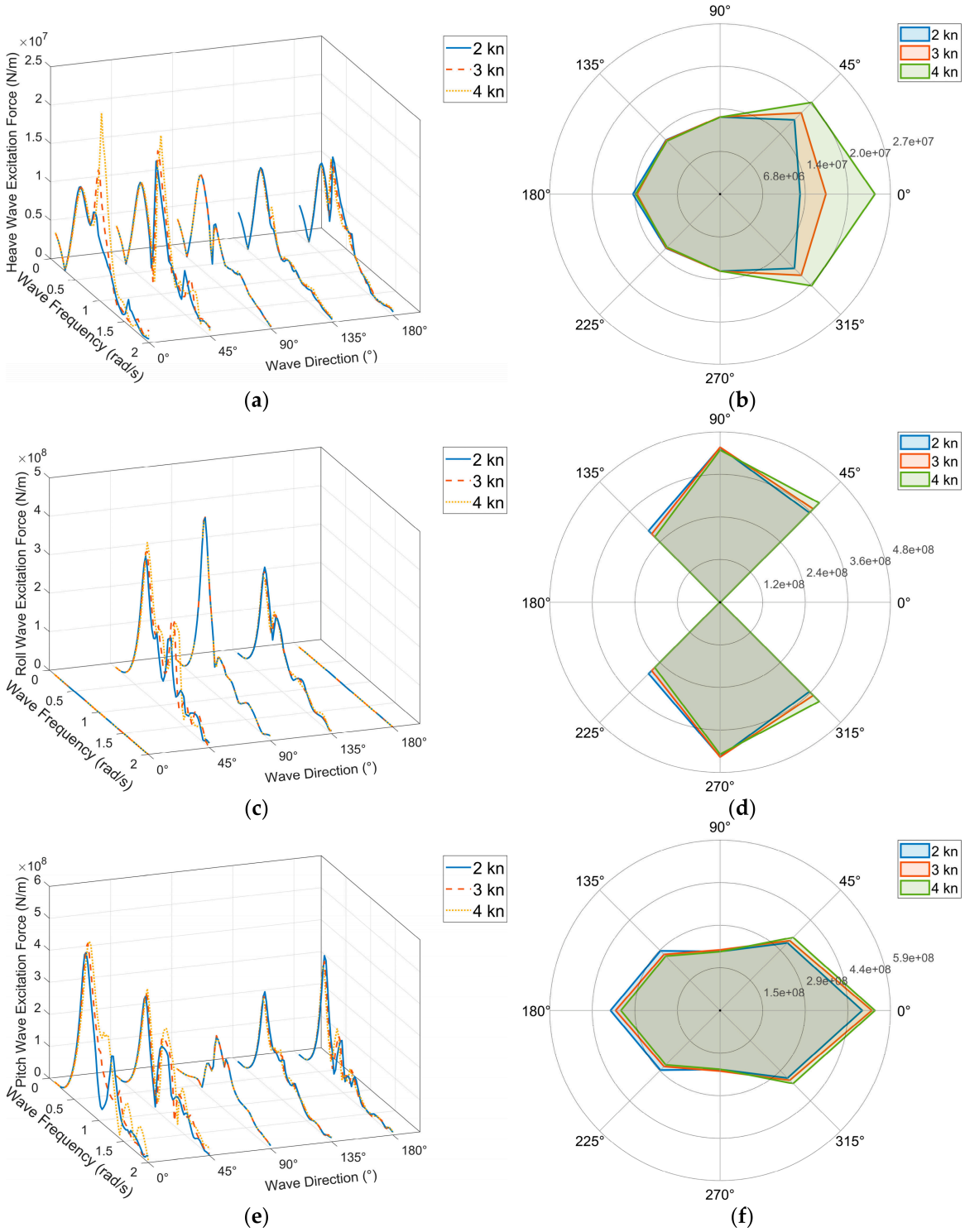

Figure 8. Wave excitation loads on FOWT at different towing speeds for double-column-forward towing: (**a**) wave excitation force in heave; (**b**) peak wave excitation force in heave; (**c**) wave excitation force in roll; (**d**) peak wave excitation force in roll; (**e**) wave excitation force in pitch; (**f**) peak wave excitation force in pitch.

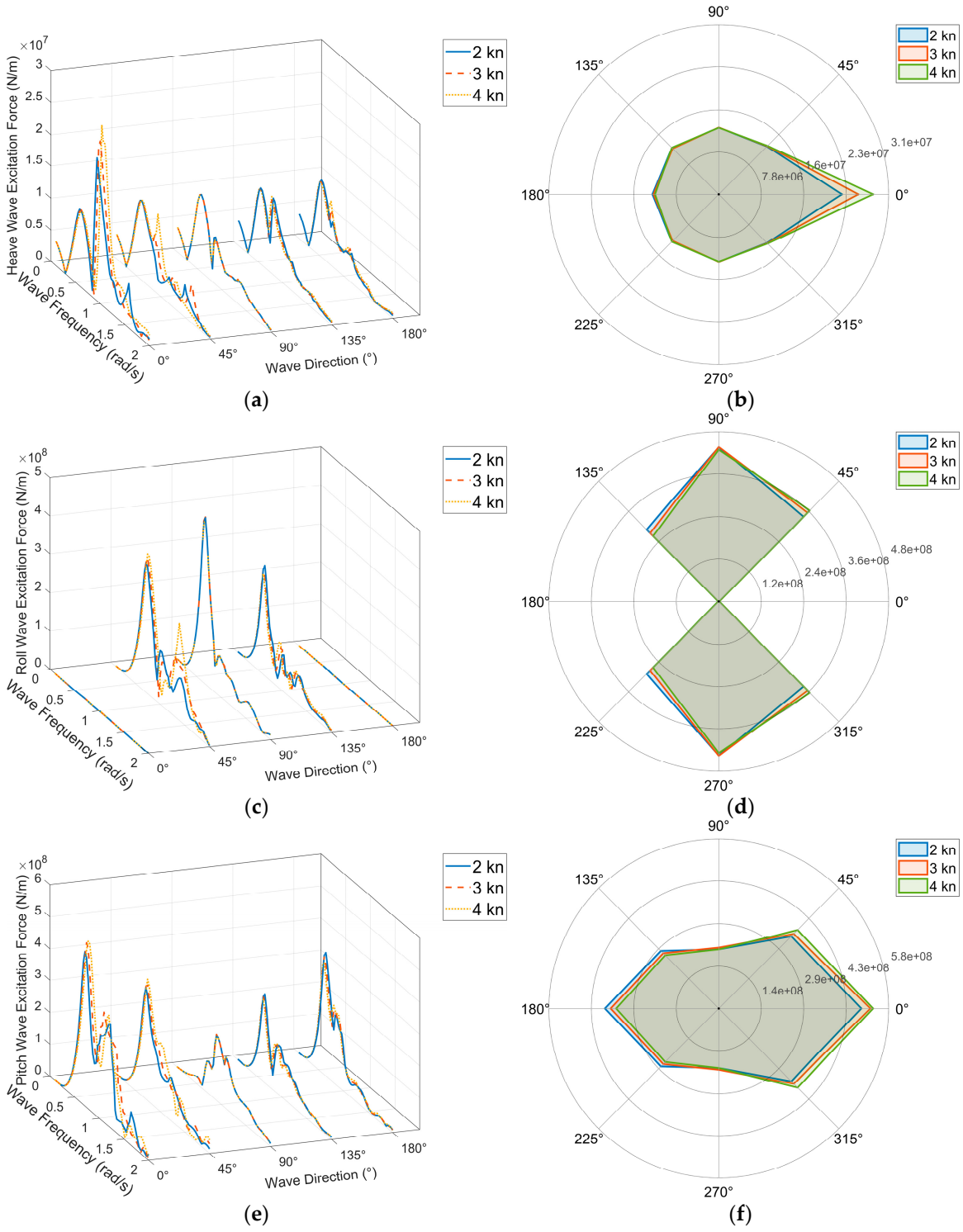

Figure 9. Wave excitation loads on FOWT at different towing speeds for single-column-forward towing: (**a**) wave excitation force in heave; (**b**) peak wave excitation force in heave; (**c**) wave excitation force in roll; (**d**) peak wave excitation force in roll; (**e**) wave excitation force in pitch; (**f**) peak wave excitation force in pitch.

The towing system was placed in a regular wave with a wave amplitude of 1.0 m, a period of 7 s, and a direction of 180°. Under these wave conditions, the floating body's roll motion response is minimal. Therefore, the heave and pitch motion responses of the FOWT were chosen to compare with frequency–time domain results. Figure 10 shows the motion response results in heave and pitch directions. It can be seen that the frequency-domain

RAO-based motion response results agree well with the time-domain results. Based on these results, the reliability of time-domain calculations can be validated.

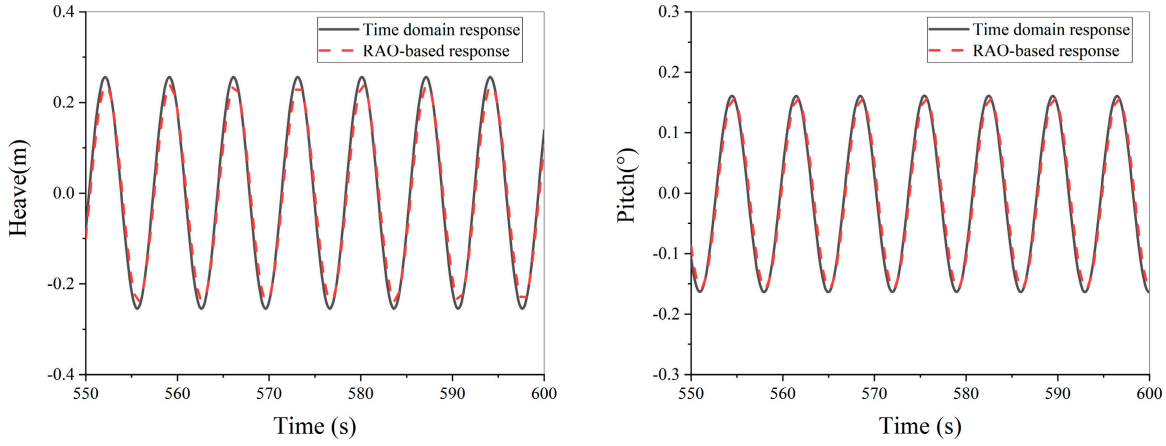

(**a**) (**b**)

Figure 10. Frequency–time domain validation: (**a**) heave; (**b**) pitch.

In addition, before subsequent calculations, a time-step convergence analysis of the towing system numerical model was required. The towing system consisting of the tugboat and FOWT connected by towlines was analyzed. The main towline has a diameter of 0.1 m and a dry weight of 41.6 kg/m. For towline length selection, according to DNV marine operation standards [42], the static clearance between the towline and the seabed should be at least 10% of the water depth, with a minimum of 5.0 m in open waters and 2.0 m in sheltered waters or calm water. In sufficiently deep waters, the towline sag should not be less than 8.0 m and not less than 13.0 m in heavy weather. The towline sag calculation formula is:

$$H = \frac{F\left[\sqrt{1+\left(\frac{0.5LW}{F}\right)^2}-1\right]}{W}, \quad (13)$$

where H is the towline sag (m); W is the weight per meter of towline in water (kg/m); L is the submerged length of the main towline (m); and F is the tugboat towing force (kn). From Equation (11), L should be at least 75.34 m. Considering the tugboat margin, the main towline length was selected as 240 m.

4.5. Towing Resistance and Towline Tension Analysis Under Calm Water Conditions

When establishing the towing system model, Morison elements and Panel elements were used to account for fluid viscous effects. Morison elements were scaled, and drag coefficients were added based on CFD results to simulate towing resistance. To verify the accuracy of the added drag coefficients, calm water resistance calculations for the FOWT were first performed. The results for different towing speeds and configurations were compared with CFD calm water resistance results.

The calm water resistance time histories are shown in Figure 11. Under calm water alone, the FOWT force is relatively stable. Before 200 s, due to the sudden application of external loads on the floating body, the resistance curve fluctuates significantly. After 200 s, the resistance basically stabilizes. Double-column-forward towing shows higher forces, with calm water resistances of 516.62 kn, 1151.67 kn, and 2108.18 kn at 2, 3, and 4 knots, respectively. For single-column-forward towing, the calm water resistances are 426.46 kn, 922.69 kn, and 1650.37 kn at 2, 3, and 4 knots, respectively.

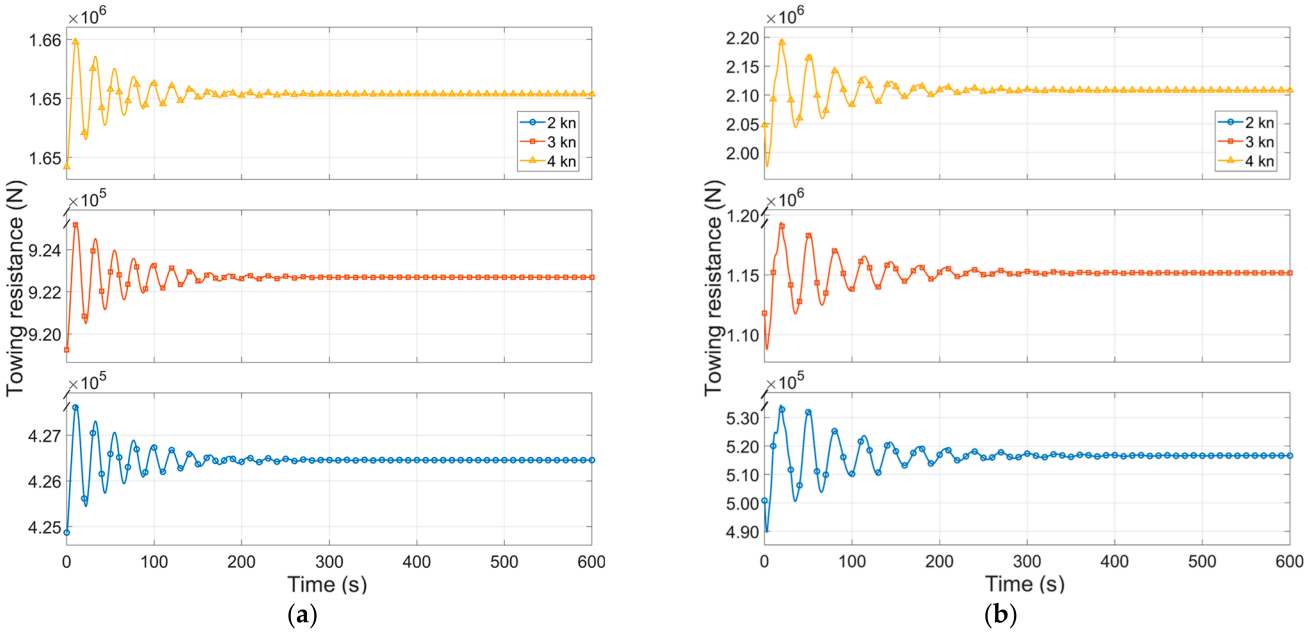

Figure 11. Calm water resistance of FOWT: (**a**) single-column-forward; (**b**) double-column-forward.

Table 3 shows a comparison of the calm water resistance results calculated by potential flow and CFD methods. The results show that the potential flow method and CFD method yield close calm water resistance results. The maximum error occurs for single-column-forward towing at 4 knots, at 1.90%. For all other conditions, the errors are within 1%, validating the effectiveness and accuracy of this drag coefficient addition method.

Table 3. Calm water resistance results from potential flow and CFD methods.

Towing Speed (kn)	Potential Flow Method Calm Water Resistance (kn)		CFD Method Calm Water Resistance (kn)		Error (%)	
	Single-Column-Forward	Double-Column-Forward	Single-Column-Forward	Double-Column-Forward	Single-Column-Forward	Double-Column-Forward
2	426.46	516.62	426.37	511.72	0.02	0.96
3	922.69	1151.67	922.51	1150.34	0.02	0.12
4	1650.37	2108.18	1619.58	2118.55	1.90	0.49

Having validated the effectiveness of the FOWT numerical model, the towing system was analyzed under calm water conditions. In towing operations, towline tension is a key indicator for assessing towing risk and dynamically reflects towing resistance. The main towline tension in the towing system was analyzed. The tension curves are shown in Figure 12. In calm water, the towing system loading is simple, and towline tension remains basically unchanged after stabilization.

For double-column-forward towing, the main towline tensions at 2, 3, and 4 knots are 519.33 kn, 1153.92 kn, and 2113.06 kn, respectively. Compared to the FOWT calm water resistance alone, these represent increases of 2.71 kn, 2.25 kn, and 4.88 kn, respectively. For single-column-forward towing, the main towline tensions at 2, 3, and 4 knots are 429.16 kn, 924.41 kn, and 1652.82 kn, respectively. Compared to the FOWT alone, these represent increases of 2.70 kn, 1.72 kn, and 2.45 kn, respectively. Towing equipment such as towlines contributes little to calm water resistance. At 2 knots with single-column-forward towing, the towing equipment accounts for the maximum proportion of total calm water resistance at 0.63%. At the same time, for double-column-forward towing, the increase in

main towline tension relative to the FOWT calm water resistance alone is higher than for single-column-forward towing. This is due to the effect of the towlines and triangle plate in the double-column-forward configuration being greater than that of the single main towline in the single-column-forward configuration.

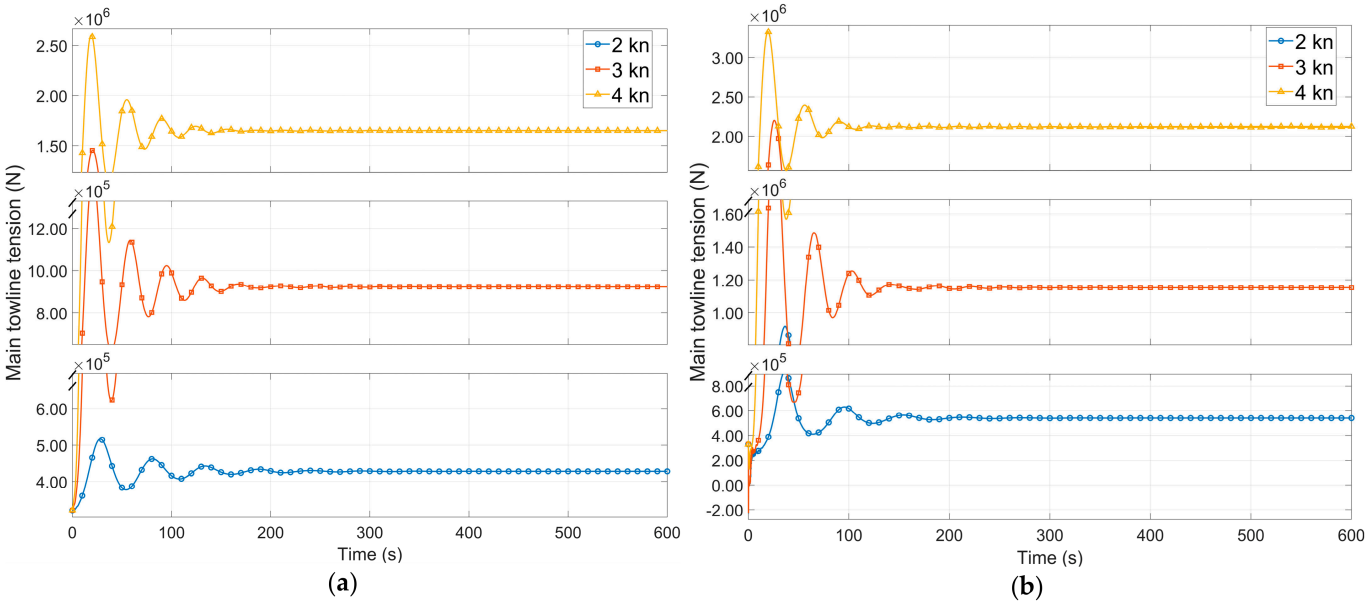

Figure 12. Main towline tension in calm water: (**a**) single-column-forward; (**b**) double-column-forward.

4.6. Towing Resistance and Towline Load Characteristics Under Regular Wave Conditions

The resistance characteristics of the towing system in regular waves were analyzed. First, resistance calculations were performed for the FOWT in regular waves with a wave height of 2.0 m, a period of 6 s, and a 180° wave direction. The wave resistance results at different towing speeds and configurations were compared with CFD wave resistance results to validate the numerical model.

Figure 13 shows the wave resistance curves based on CFD and potential flow methods. The stable segments of the two resistance curves were extracted and aligned. The curves show good agreement under different conditions. Resistance varies periodically, with the variation period consistent with the wave encounter period. As towing speed increases, the floating wind turbine encounters more waves in the same time period, and the force becomes more frequent. The mean resistance values over multiple wave periods are shown in Table 4. The mean wave resistance errors between CFD and potential flow methods are all within 5%, validating the effectiveness of the FOWT hydrodynamic model.

Table 4. Mean wave resistance from potential flow and CFD methods.

Towing Speed (kn)	Potential Flow Method Wave Resistance (kn)		CFD Method Wave Resistance (kn)		Error (%)	
	Single-Column-Forward	Double-Column-Forward	Single-Column-Forward	Double-Column-Forward	Single-Column-Forward	Double-Column-Forward
2	503.47	631.97	505.73	621.04	0.45	1.76
3	1002.98	1275.20	1039.18	1289.51	3.48	1.11
4	1696.16	2230.07	1670.55	2311.35	1.53	3.52

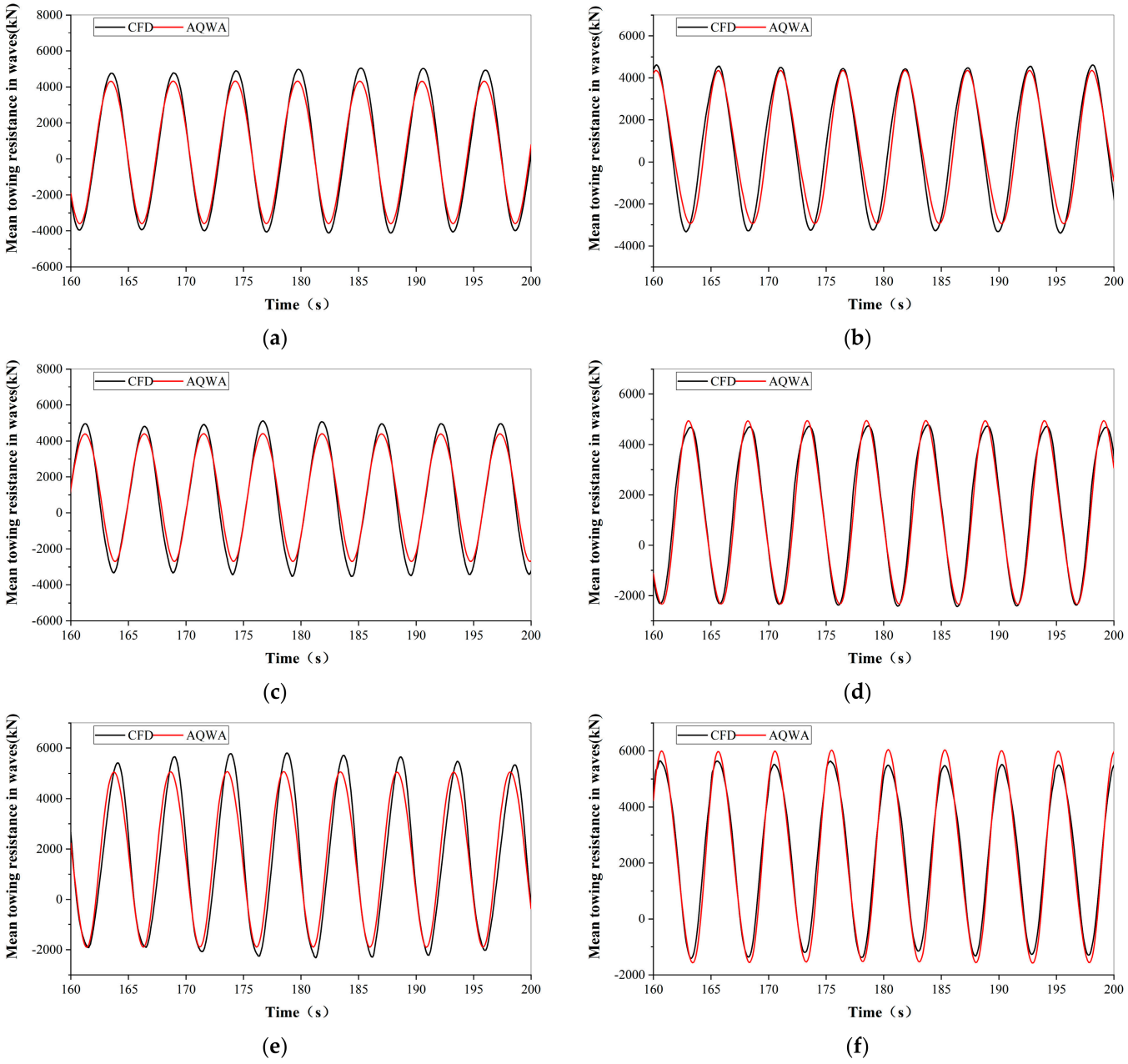

Figure 13. Comparison of wave resistance between potential flow and CFD methods: (**a**) single-column-forward (2 kn); (**b**) double-column-forward (2 kn); (**c**) single-column-forward (3 kn); (**d**) double-column-forward (3 kn); (**e**) single-column-forward (4 kn); (**f**) double-column-forward (4 kn).

The towing system was analyzed in regular waves. Figure 14 shows a comparison between the main towline tension and the FOWT force. It can be seen that under both column configurations, wave action causes significant periodic fluctuations in FOWT force. The towline effectively reduces the amplitude of these fluctuations, making the loads transmitted to the tugboat more stable. As towing speed increases, both the mean wave load on the turbine and the mean main towline tension increase accordingly, and the overall force level of the system rises. However, within the studied speed range and towing configurations, the cushioning effect of the towline on dynamic loads does not show significant weakening.

At the same time, the mean main towline tension and the mean wave resistance on the FOWT were analyzed. The results are summarized in Table 5. The relative errors between

the mean main towline tension and the mean wave resistance directly experienced by the FOWT are all less than 2%. This indicates that the main towline tension can accurately represent the towing resistance level of the FOWT in these wave conditions.

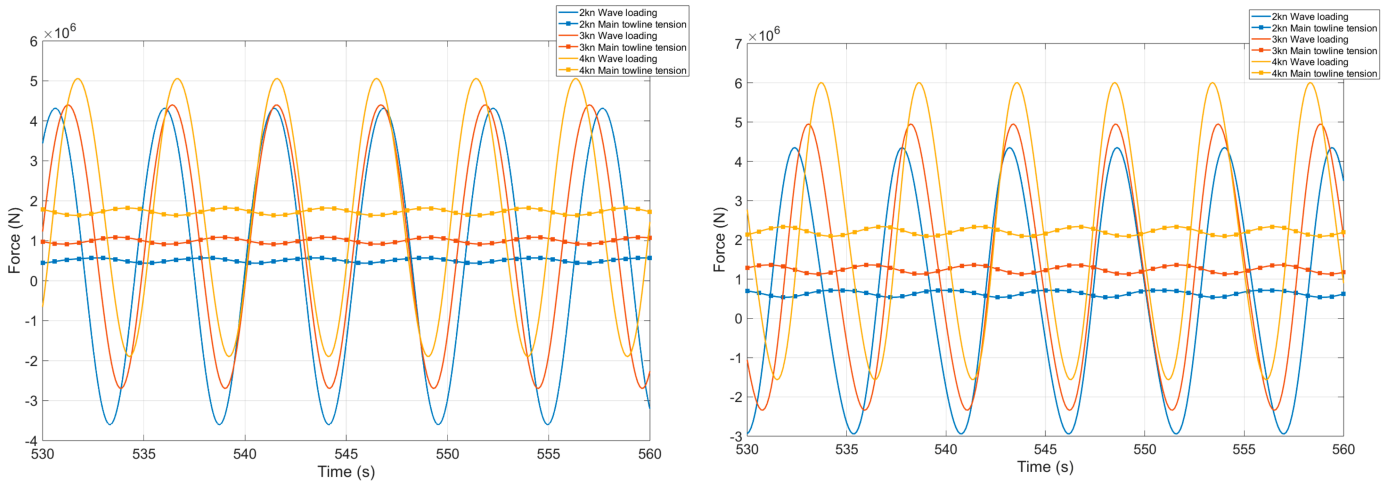

Figure 14. Comparison of main towline tension and FOWT force among different ship speeds: (**a**) single-column-forward; (**b**) double-column-forward.

Table 5. Mean main towline tension and FOWT force in wave environment.

Towing Speed (kn)	FOWT Force (kn)		Main Towline Tension (kn)		Error (%)	
	Single-Column-Forward	Double-Column-Forward	Single-Column-Forward	Double-Column-Forward	Single-Column-Forward	Double-Column-Forward
2	503.47	631.97	511.59	620.41	1.61	1.83
3	1002.98	1275.20	1001.81	1252.16	0.12	1.81
4	1696.16	2230.07	1728.25	2214.21	1.89	0.71

Compared to calm water towing conditions, the relationship between main towline tension and FOWT force in wave conditions shows significant differences. Under calm water conditions, the main towline tension shows a simple increasing trend relative to the FOWT force. However, in wave conditions, due to the significant motion response of the FOWT under wave action, towline tension is affected by the coupling between structural motion and wave loads. Its variation characteristics are more complex, and it no longer shows a simple increasing trend relative to the FOWT force. Overall, the main towline tension can still effectively reflect the overall towing resistance level of the FOWT. In subsequent research, main towline tension values will be used to represent towing resistance.

To investigate the wave-added resistance effect, the wave resistance of the FOWT towing system was compared with the calm water resistance. The mean main towline tension was analyzed, and the results are shown in Table 6. Under regular waves with a wave height of 2.0 m, a period of 6 s, and a 180° wave direction, the absolute values of wave-added resistance at different towing speeds are relatively close. For single-column-forward towing, the wave-added resistances at 2, 3, and 4 knots are 82.43 kn, 77.40 kn, and 75.43 kn, respectively. The mean wave-added resistance across the three speeds is 78.42 kn. For double-column-forward towing, the wave-added resistance is larger than that for single-column towing. The mean wave-added resistance is 100.16 kn, approximately 27.71% higher than for single-column towing.

Table 6. Mean main towline tension in wave and calm water environments.

Towing Speed (kn)	Single-Column-Forward Main Towline Tension Mean (kn)			Double-Column-Forward Main Towline Tension Mean (kn)		
	Calm Water	Wave	Wave-Added	Calm Water	Wave	Wave-Added
2	429.16	511.59	82.43	519.33	620.41	101.08
3	924.41	1001.81	77.40	1153.92	1252.16	98.24
4	1652.82	1728.25	75.43	2113.06	2214.21	101.15

It can be seen that towing speed has a relatively small effect on wave-added resistance. To further investigate the wave-added resistance characteristics of towing resistance, parametric analysis was conducted. First, the wave-added resistance of towing resistance under different regular wave periods was studied. Four sets of towing regular wave conditions were established. All conditions had a wave height of 2.0 m and a load direction of 180°. Wave periods of 6 s, 7 s, 8 s, 9 s, and 10 s were used for comparative calculations. The wave-added resistance characteristics under different regular wave periods were further investigated. Each wave condition considered both the two towing configurations and three towing speeds.

The wave-added resistance results for each condition were analyzed, and the results are shown in Table 7. The results show that wave period has a significant effect on wave-added resistance. After the 7 s period, the wave-added resistance at each towing speed generally shows a trend of first increasing and then decreasing. At the same time, the absolute differences in wave-added resistance at different towing speeds are no longer as close as at the 6 s period, but show larger variations. In addition, at the high wave period of 10 s, the single-column-forward wave-added resistance even exceeds that of double-column-forward towing.

Figure 15 shows a comparison of frequency-domain surge wave excitation loads and wave-added resistance for the 180° wave direction. The frequency-domain wave excitation loads show significant fluctuations under all towing speed conditions. Correspondingly, wave-added resistance also shows certain synchronization with period variation, and the overall trend correlates well with the wave excitation load changes. Comparing different towing configurations, under the same towing speed, the frequency-domain wave excitation load level for double-column-forward towing is generally higher than that for single-column-forward towing. The corresponding wave-added resistance amplitude is also relatively large. However, at high wave periods, the frequency-domain wave excitation load level for double-column-forward towing drops significantly, and the corresponding wave-added resistance is also smaller than that for single-column-forward towing. Due to the motion and coupling effects of the FOWT towing system, the wave excitation loads do not fully reflect the changes in wave-added resistance. However, overall, the frequency-domain surge wave excitation loads and wave-added resistance show high correlation in variation characteristics. The wave periods with greater impact on towing resistance can be preliminarily identified through surge wave excitation loads.

The wave-added resistance of towing operations under four sets of towing regular wave conditions was studied. All conditions had a wave period of 7 s and a load direction of 180°. Wave heights of 2.5 m, 3.0 m, 3.5 m, and 4.0 m were used for comparative calculations. Each wave condition considered both towing configurations and three towing speeds: 2, 3, and 4 knots.

The wave-added resistance results for each condition are summarized in Table 8. Under the same towing speed, wave-added resistance shows a significant increasing trend with wave height. This trend is consistent for both single-column and double-column-

forward towing. Comparing different structural configurations, the wave-added resistance of the double-column configuration is significantly higher than that of the single-column configuration under all towing speeds and wave heights. As wave height increases, the difference between the two gradually expands. In addition, under the same wave height, the overall difference in wave-added resistance at different towing speeds for single-column-forward towing is relatively small. At the 4.0 m wave height, the maximum difference does not exceed 5%. However, for double-column-forward towing, wave-added resistance gradually decreases with increasing towing speed, consistent with the trend of frequency-domain wave excitation loads. The differences in wave-added resistance at different towing speeds are relatively large, with a maximum difference of 27.27%.

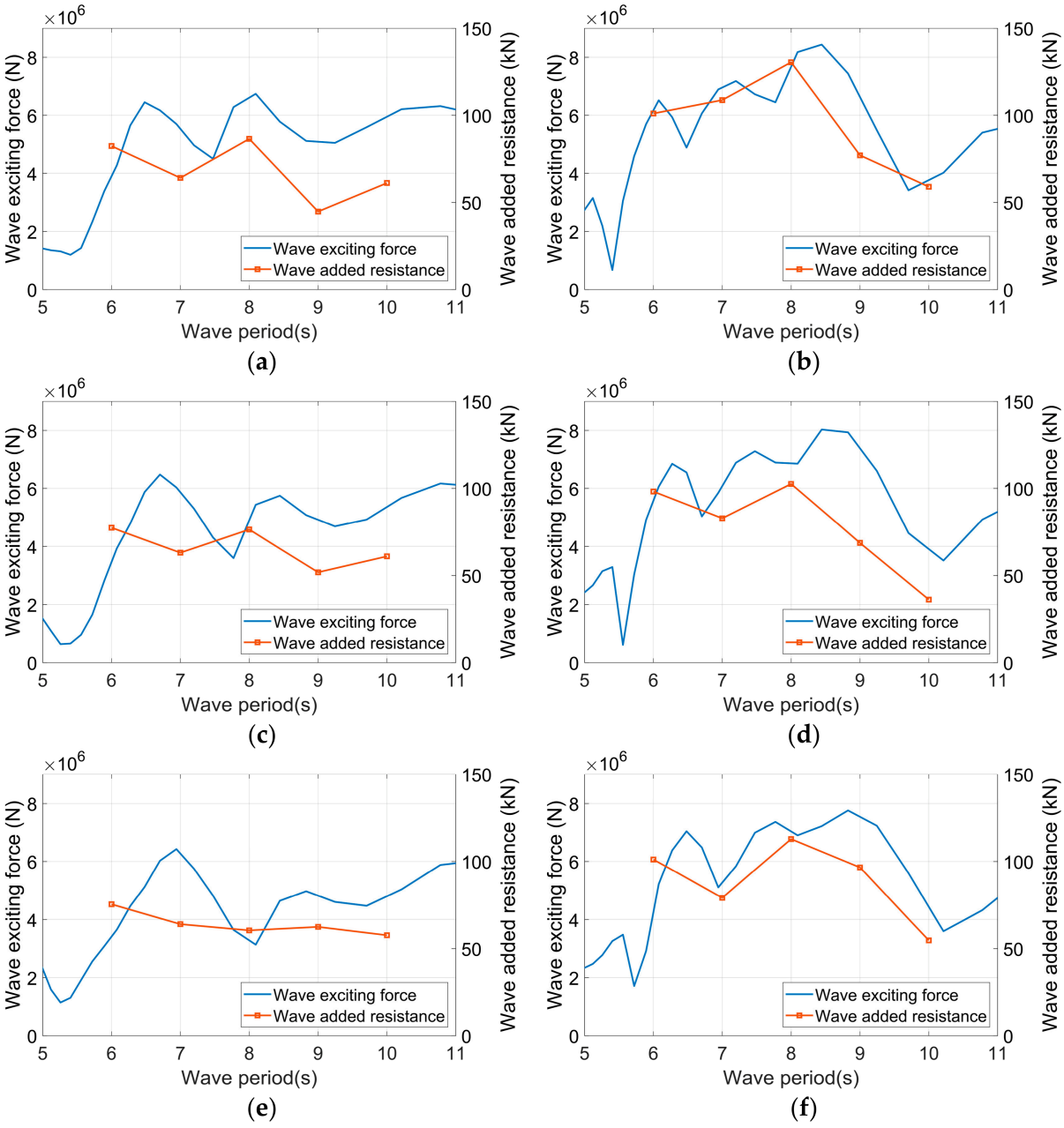

Figure 15. Comparison of frequency-domain wave excitation loads and wave-added resistance: (**a**) single-column-forward (2 kn); (**b**) double-column-forward (2 kn); (**c**) single-column-forward (3 kn); (**d**) double-column-forward (3 kn); (**e**) single-column-forward (4 kn); (**f**) double-column-forward (4 kn).

To further analyze the trend and incremental characteristics of wave-added resistance with wave height, Figure 16 shows the wave-added resistance and the increment between adjacent wave height conditions under different towing speeds and configurations. From the increments between adjacent wave height conditions, as wave height increases from 2.0 m to 4.0 m, the wave-added resistance increment generally shows a gradually increasing trend. In larger wave conditions, the sensitivity of wave-added resistance to wave height changes is significantly enhanced. At the same towing speed, the resistance increment for double-column-forward towing is generally higher than that for single-column-forward towing. However, this difference decreases somewhat as wave height increases.

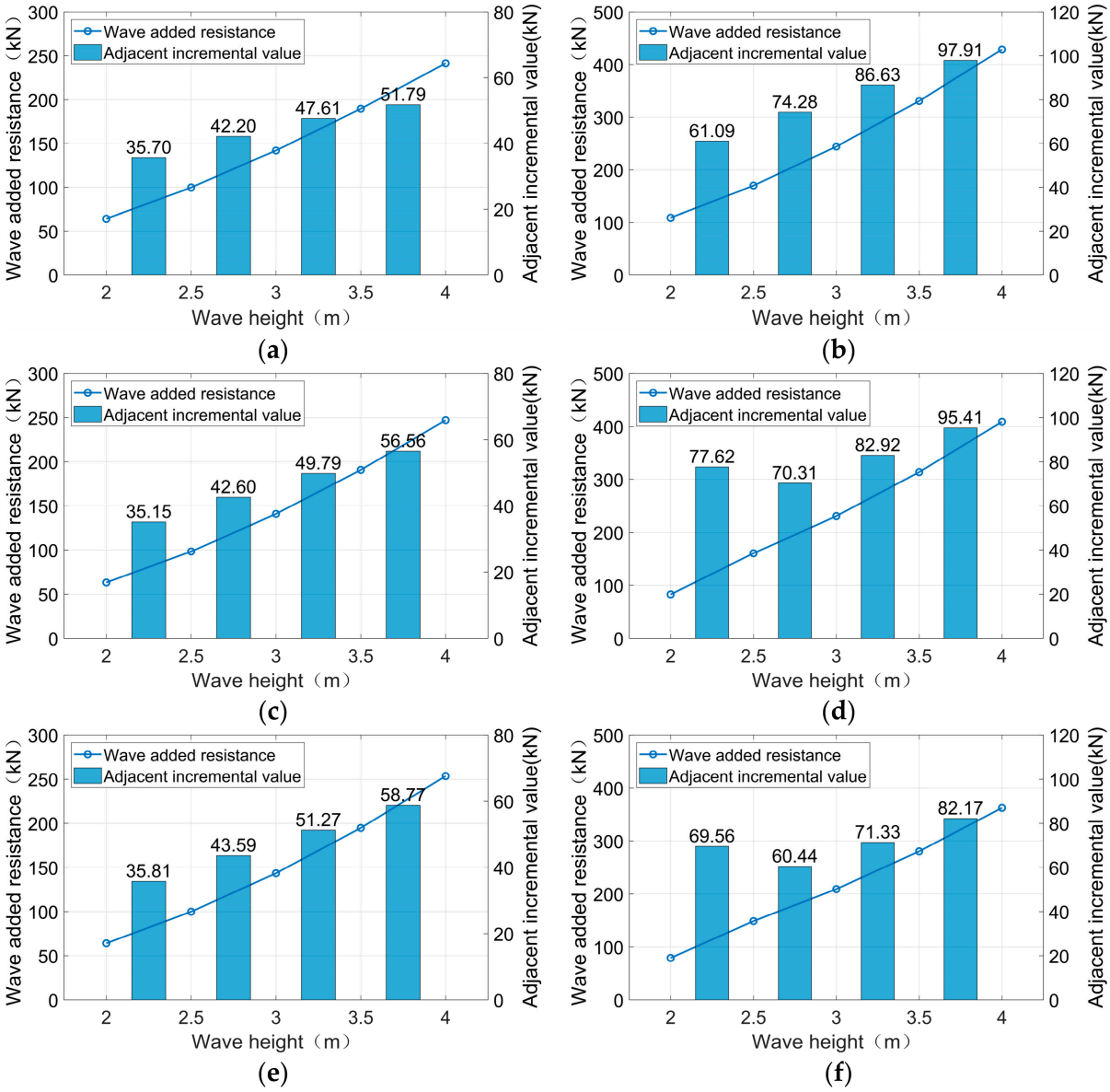

Figure 16. Wave-added resistance at different wave heights and towing resistance increments between adjacent wave heights: (**a**) single-column-forward (2 kn); (**b**) double-column-forward (2 kn); (**c**) single-column-forward (3 kn); (**d**) double-column-forward (3 kn); (**e**) single-column-forward (4 kn); (**f**) double-column-forward (4 kn).

Table 7. Wave-added resistance under different regular wave periods.

Wave Period (s)	2 kn Towing Speed Wave-Added Resistance (kn)		3 kn Towing Speed Wave-Added Resistance (kn)		4 kn Towing Speed Wave-Added Resistance (kn)	
	Single-Column-Forward	Double-Column-Forward	Single-Column-Forward	Double-Column-Forward	Single-Column-Forward	Double-Column-Forward
6	82.43	101.08	77.40	98.24	75.43	101.15
7	64.10	108.79	63.15	82.82	64.08	79.12
8	86.55	130.53	76.40	102.61	60.51	112.92
9	44.77	77.11	51.89	68.74	62.52	96.57
10	61.18	59.00	61.07	36.21	57.72	54.76

Table 8. Wave-added resistance under different regular wave heights.

Wave Height (m)	2 kn Towing Speed Wave-Added Resistance (kn)		3 kn Towing Speed Wave-Added Resistance (kn)		4 kn Towing Speed Wave-Added Resistance (kn)	
	Single-Column-Forward	Double-Column-Forward	Single-Column-Forward	Double-Column-Forward	Single-Column-Forward	Double-Column-Forward
2.0	64.10	108.79	63.15	82.82	64.08	79.12
2.5	99.81	169.88	98.30	160.44	99.89	148.68
3.0	142.01	244.16	140.90	230.75	143.48	209.12
3.5	189.62	330.79	190.70	313.67	194.75	280.45
4.0	241.40	428.70	247.26	409.08	253.52	362.61

5. Discussion

This study proposes a viscous correction strategy for the potential flow method to enhance the numerical prediction performance of towing hydrodynamics for semi-submersible floating offshore wind turbines. Different from pure CFD simulation, the modified potential flow model aims to achieve a good balance between computational efficiency and calculation accuracy, which is particularly suitable for parametric analysis in the preliminary towing design stage.

To establish a feasible and efficient numerical framework, several reasonable simplifications and assumptions have been adopted in the present work. The numerical validation is conducted under regular wave conditions with dominant head sea scenarios. The hydrodynamic calculation ignores aerodynamic loads and current effects and only considers typical rigid-body motion modes, including heave, roll and pitch. The upper tower structure is not included in the fluid calculation domain, and the entire platform is treated as a rigid body during the towing process. These simplified settings are commonly adopted in preliminary hydrodynamic evaluations of floating wind turbine towing problems and can effectively reduce the computational cost.

Despite the satisfactory overall accuracy verified in this study, the existing simplifications inevitably introduce numerical errors and application limitations. The deviation between the predicted results and benchmark data is mainly attributed to the neglect of nonlinear flow separation, complex wave–structure coupling effects, and multi-degree-of-freedom motion coupling interference. Accordingly, the current method is only applicable to limited towing speed ranges and regular wave environments, and its adaptability to complex marine conditions remains to be further verified.

In practical engineering applications, the proposed correction method can provide reliable hydrodynamic references for the wet-towing design of floating wind turbines. It supports the rapid evaluation of towing resistance characteristics and helps designers

formulate reasonable towing schemes, select appropriate tugboat configurations, and optimize marine operation weather windows. Compared with traditional overly conservative empirical estimation methods, the present numerical strategy can effectively avoid excessive safety margins, which is beneficial to improving the economy and environmental friendliness of offshore towing operations.

There is still room for further improvement and expansion in this research. Subsequent studies can incorporate irregular wave conditions, oblique wave loads, and coupled aerodynamic–hydrodynamic effects to establish a more comprehensive numerical system. Moreover, future work can further explore the influence of flexible structural deformation, towline dynamic characteristics, and variable marine environments on towing hydrodynamic performance, so as to form a more universal and robust prediction method for floating wind turbine towing resistance.

6. Conclusions

This study investigates the towing resistance characteristics of the IEA-15MW semi-submersible floating offshore wind turbine (FOWT) under wave conditions using both CFD and a viscous-potential flow correction method, with the aim of improving the efficiency and sustainability of wet-towing operations. The effects of towing speed, towing configuration, and wave parameters are systematically analyzed. The main findings are as follows:

(a) CFD simulations show that the wave-resistance response period coincides with the encounter period; higher towing speeds lead to increased forces on the FOWT. The double-column-forward configuration consistently exhibits higher resistance than the single-column-forward configuration across all speeds, providing a quantitative basis for selecting the more energy-efficient towing arrangement.

(b) Based on CFD free-decay results, viscous damping corrections (heave, roll, and pitch) are applied to the potential-flow model, and drag coefficients are introduced through Morison elements to establish a coupled tugboat–FOWT–towing-line numerical model. Frequency-domain analysis reveals that towing speed has a minor influence on added mass and radiation damping. However, wave-excitation loads increase with speed in following seas and decrease in head seas; the single-column configuration is more sensitive to following waves, while the double-column configuration shows stronger responses to oblique waves.

(c) Time-domain validation demonstrates that the corrected potential-flow model predicts calm water resistance within 2% of CFD results and mean wave resistance within 5%, confirming the effectiveness and accuracy of the correction method. In calm water, towing accessories (lines and triangular plate) contribute less than 1% to the total resistance, though the increase in main towline tension relative to the FOWT force is slightly higher for the double-column configuration due to the additional rigging.

(d) The CFD-calibrated potential flow model reproduced calm water towing resistance with a maximum deviation of 1.90% and mean regular wave resistance with a maximum deviation of 3.52%. The difference between mean main towline tension and mean FOWT resistance was 0.12–1.89% in regular waves. Towing lines and the triangular plate contributed no more than 0.63% of the calm water resistance. Mean main towline tension can therefore represent mean towing resistance within the tested conditions, but it should not be used as a substitute for instantaneous platform force or peak cable load.

(e) At 2–4 kn, the double column forward configuration increased calm water resistance by 20.0–30.8% and regular wave resistance by 22.8–38.4% relative to the single column forward configuration. Under the 2 m, 6 s regular head wave, its mean wave added

resistance was 100.16 kn, compared with 78.42 kn for the single column forward configuration. The dependence on wave period was nonmonotonic and varied with towing speed and configuration. Wave added resistance increased strongly and nonlinearly as wave height rose from 2 to 4 m.

The method is suitable for comparative hydrodynamic screening under the modeled low wind, regular wave conditions. Independent experiments, irregular wave spectra, oblique wave time domain cases, higher towing speeds, aerodynamic loading, and towline parameter uncertainty require further investigation before the method is applied as a general design procedure. Absolute fuel consumption and emission reductions were not calculated in this study. However, from a sustainability perspective, the proposed framework offers practical value in three respects: it allows tugs to be allocated to actual resistance demand rather than conservative upper bounds, avoiding excess fuel consumption and emissions; its parametric findings provide quantitative guidance for energy-efficient towing layouts and weather windows; and, by reproducing viscous-flow accuracy at potential-flow cost, it makes sustainability-oriented optimization feasible at the scale of entire installation campaigns. Together, these contributions support safer, cheaper, and lower-carbon deployment of floating offshore wind energy.

Author Contributions: Conceptualization, N.C. and S.Y.; methodology, software, X.J. and Y.T.; validation, C.T., S.Y. and R.L.; formal analysis and investigation, R.L., X.J. and Y.T.; data curation, N.C., and Y.T.; writing—original draft preparation, N.C.; writing—review and editing, C.T.; visualization, R.L. and X.J.; resources, supervision, project administration and funding acquisition, M.C. All authors have read and agreed to the published version of the manuscript.

Funding: The authors gratefully acknowledge the financial support from the National Natural Science Foundation of China and "the Fundamental Research Funds for the Central Universities" (Grant No. U25A20373).

Institutional Review Board Statement: Not applicable.

Informed Consent Statement: Not applicable.

Data Availability Statement: The original contributions presented in this study are included in the article. Further inquiries can be directed to the corresponding author.

Conflicts of Interest: Authors Ning Cui and Sheng Yang are employed by the company CNOOC Shenzhen Offshore Engineering Solutions Co., Ltd. The remaining authors declare that the research was conducted in the absence of any commercial or financial relationships that could be construed as potential conflicts of interest.

References

1. Khan, M.Z.A.; Khan, H.A.; Aziz, M. Harvesting Energy from Ocean: Technologies and Perspectives. *Energies* **2022**, *15*, 3456. [CrossRef]
2. Chen, X.X.; Wang, T.Y.; Cai, C.; Liu, J.S.; Gao, X.X.; Guo, N.Z.; Li, Q.G. A Review of Experiment Methods, Simulation Approaches and Wake Characteristics of Floating Offshore Wind Turbines. *J. Mar. Sci. Eng.* **2025**, *13*, 208. [CrossRef]
3. Ma, X.M.; Li, M.X.; Li, W.Q.; Liu, Y.Q. Overview of Offshore Wind Power Technologies. *Sustainability* **2025**, *17*, 596. [CrossRef]
4. Ramachandran, R.C.; Serraris, J.J.; Montfort, J.H.; De Ridder, E.J.; Desmond, C.; Murphy, J. Towing Analysis and Validation of a Fully Assembled Floating Offshore Wind Turbine Based on an Experimental Study. *J. Mar. Sci. Eng.* **2024**, *12*, 689. [CrossRef]
5. Liu, X.L.; Liu, H.N.; Wu, J.B.; Wu, H.X.; Zhang, T.; Zhao, W.Q.; Tan, P.H. Filter-based ultralow-frequency Raman measurement down to 2 cm(-1) for fast Brillouin spectroscopy measurement. *Rev. Sci. Instrum.* **2017**, *88*, 053110. [CrossRef] [PubMed]
6. Yin, D.C.; Indergård, R.; Lie, H.; Braaten, H. Experimental Investigation of Towing of a Semi-submersible Floating Offshore Wind Turbine. *Eera Deep. Conf.* **2024**, *2024*, 2875. [CrossRef]
7. Chen, M.; Chen, Y.; Li, T.; Tang, Y.; Ye, J.; Zhou, H.; Ouyang, M.; Zhang, X.; Shi, W.; Sun, X. Analysis of the wet-towing operation of a semi-submersible floating wind turbine using a single tugboat. *Ocean. Eng.* **2024**, *299*, 117354. [CrossRef]

8. Chen, M.; Liu, S.; Jiang, X.; Hu, M.; Li, Z.; Jiang, J.; Li, J. Comparative analysis of fully-coupled towing simulation for a 15MW floating wind turbine using FAST2AQWA method. *Ocean. Eng.* **2026**, *347*, 124003. [CrossRef]
9. Ramachandran, R.; Otter, A.; Serraris, J.; Ridder, E.d.; Desmond, C.; Murphy, J. A study of the towing characteristics of a semi-submersible floating offshore wind platform. *J. Phys. Conf. Ser.* **2023**, *2626*, 012043. [CrossRef]
10. Tang, Y.; Chen, M.; Chen, Y.; Yu, N.; Wu, J.; Jiang, X.; Liu, S.; Yuan, Z.-M. Coupled aero-hydro-servo-elastic analysis of advanced wet-towing schemes for the IEA 15MW floating wind turbine. *Ocean. Eng.* **2026**, *356*, 125321. [CrossRef]
11. Davis, S.; Viselli, A.; Verma, A.J.E. Experimental and numerical study of a towing test for a barge-type floating offshore wind turbine. *Energies* **2025**, *18*, 5228. [CrossRef]
12. Feng, R.; Fang, J.; Pan, T.; Huang, Z.; Sheng, Y.; Fan, T.J.E. Experimental and Simulation Research on the Motion Response of a Floating Offshore Wind Turbine During Wet-Towing Operation. *Energies* **2026**, *19*, 863. [CrossRef]
13. Le, C.; Ren, J.; Wang, K.; Zhang, P.; Ding, H. Towing performance of the submerged floating offshore wind turbine under different wave conditions. *J. Mar. Sci. Eng.* **2021**, *9*, 633. [CrossRef]
14. Ferreira, D.N.; Gonçalves, P.M.; Baltazar, J. Towing Simulations of a Semi-Submersible Floating Wind Platform Using RANS-based CFD. *J. Phys. Conf. Ser.* **2026**, *3224*, 082043. [CrossRef]
15. Zhang, P.; Zhao, X.; Ding, H.; Le, C.J.M.S. The wet-towing resistance of the composite bucket foundation for offshore wind turbines. *Mar. Struct.* **2021**, *80*, 103089. [CrossRef]
16. Roberts, A.; Le Pivert, F.; Kazemi, S.; Tosdevin, T.; López-Santander, A.; Craven, M.J.; Johanning, L.J.O.E. Scale model and ship simulator towing of the IEA 15 MW wind turbine on the UMaine VolturnUS-S platform. *Ocean. Eng.* **2025**, *336*, 121732. [CrossRef]
17. Ramachandran, R.; Serraris, J.; de Ridder, E.; Desmond, C.; Murphy, J. An analysis of floating wind turbine towing operations using OpenFAST. *J. Phys. Conf. Ser.* **2024**, *2875*, 012035. [CrossRef]
18. Tang, Y.; Chen, M.; Yu, N.; Jiang, Y.; Jiang, X.; Song, F.; Dai, S.; Huang, Z. An efficient hydrodynamic-structure unified state-space model for the coupled dynamics during floating wind turbine wet-towing construction. *Phys. Fluids* **2026**, *38*, 088137. [CrossRef]
19. Le Pivert, F.; López-Santander, A.; Craven, M.J.; Roberts, A. Routing optimisation for towing a floating offshore wind turbine under weather constraints. *Ocean. Eng.* **2024**, *305*, 118025. [CrossRef]
20. Lian, J.J.; Xiao, T.R.; Liu, D.M.; Ye, F.D.; Xiong, D.Z. The offshore prefabrication and semi-wet towing of a bucket foundation for offshore wind turbines. *Ocean. Eng.* **2023**, *285*, 115354. [CrossRef]
21. Wang, H.; Yang, Y.; Guo, Y.; Lian, J. Influence of Heave Plate on the Dynamic Response of a 10 MW Semisubmersible Floating Platform. *J. Mar. Sci. Eng.* **2024**, *12*, 2156. [CrossRef]
22. Wang, Z.; Li, T.; Jin, Q.; Wang, S.; Huang, X.; Qi, J.; Guedes Soares, C. Numerical study on hydrodynamic characteristics of the ship lock entry process under both constant-speed and fixed-thrust conditions. *Phys. Fluids* **2026**, *38*, 013112. [CrossRef]
23. Wang, Z.; Li, T.; Mei, Q.; Wang, S.; Zhao, X.; Qi, J.; Guedes Soares, C. Study on total resistance of ships navigating in shallow water. *Ocean. Eng.* **2026**, *343*, 123463. [CrossRef]
24. Hmedi, M.; Uzunoglu, E.; Medina-Manuel, A.; Mas-Soler, J.; Vittori, F.; Pires, O.; Azcona, J.; Souto-Iglesias, A.; Guedes Soares, C. Experimental Analysis of CENTEC-TLP Self-Stable Platform with a 10 MW Turbine. *J. Mar. Sci. Eng.* **2022**, *10*, 1910. [CrossRef]
25. Yousefifard, M.; Nowruzi, H. Hydrodynamic performance of sandglass-type floating body with damping appendages. *Ocean. Eng.* **2024**, *309*, 118579. [CrossRef]
26. Qu, X.; Jiang, Y.; Zhang, R.; Long, F. A Deep Reinforcement Learning-Based Path-Following Control Scheme for an Uncertain Under-Actuated Autonomous Marine Vehicle. *J. Mar. Sci. Eng.* **2023**, *11*, 1762. [CrossRef]
27. Chen, M.; Ouyang, M.; Li, T.; Zou, M.; Ye, J.; Tian, X. Numerical modelling of a catamaran float-over deck installation for a spar platform with complex hydrodynamic interactions and mechanical couplings. *Ocean. Eng.* **2023**, *287*, 115905. [CrossRef]
28. Chen, M.; Ouyang, M.; Guo, H.; Zou, M.; Zhang, C. A Coupled Hydrodynamic–Structural Model for Flexible Interconnected Multiple Floating Bodies. *J. Mar. Sci. Eng.* **2023**, *11*, 813. [CrossRef]
29. Chen, M.; Xiao, P.; Zhou, H.; Li, C.B.; Zhang, X. Fully Coupled Analysis of an Integrated Floating Wind-Wave Power Generation Platform in Operational Sea-States. *Front. Energy Res.* **2022**, *10*, 2022. [CrossRef]
30. Bartosik, A.S. Advances in Numerical Heat Transfer and Fluid Flow. *Energies* **2024**, *17*, 2108. [CrossRef]
31. Yang, Q.; Dong, J.; Xing, T.J.; Zhang, Y.; Guan, Y.; Liu, X.L.; Tian, Y.; Yu, P. RANS-Based Modelling of Turbulent Flow in Submarine Pipe Bends: Effect of Computational Mesh and Turbulence Modelling. *J. Mar. Sci. Eng.* **2023**, *11*, 336. [CrossRef]
32. Ryu, S. A Mathematically Exact and Well-Determined System of Equations to Close Reynolds-Averaged Navier–Stokes Equations. *Mathematics* **2023**, *11*, 4926. [CrossRef]
33. Menter, F.; Hüppe, A.; Matyushenko, A.; Kolmogorov, D. An Overview of Hybrid RANS–LES Models Developed for Industrial CFD. *Appl. Sci.* **2021**, *11*, 2459. [CrossRef]
34. Li, T.T.; Wang, Y.J.; Li, Y.; Wang, B.; Liu, Q.H.; Chen, X. Feasibility of the Northern Sea Route: Impact of Sea Ice Thickness Uncertainty on Navigation. *J. Mar. Sci. Eng.* **2024**, *12*, 1078. [CrossRef]
35. Reyes, C.C.M.; Huang, Z.H. A Revisit of Parametrizing Energy Dissipation Caused by Vortex Shedding at Thin-Plate Edges in Potential-Flow Models. *Water* **2026**, *18*, 608. [CrossRef]

36. Noblesse, F.; He, J.Y. Beyond Accuracy: Importance of Practical Potential-Flow Tools in Ship Hydrodynamics Design. *J. Mar. Sci. Eng.* **2026**, *14*, 366. [CrossRef]
37. Nair, A.; Huang, L.F.; Verdin, P.G. Computational Fluid Dynamics and Potential Flow Modelling Techniques for Floating Photovoltaic Systems: A Systematic Review. *Symmetry* **2025**, *17*, 1508. [CrossRef]
38. Yang, S.; Li, Y.J.; Wang, Z.A.; Zhao, Z.J.; Wang, J.Q.; Zhou, L. An Optimized Four-Float Semi-Submersible Offshore Wind Turbine Platform: Hydrodynamic and Motion Response Evaluation. *J. Mar. Sci. Eng.* **2026**, *14*, 807. [CrossRef]
39. Lin, Y.H.; Yang, C.H. Hydrodynamic Simulation of the Semi-Submersible Wind Float by Investigating Mooring Systems in Irregular Waves. *Appl. Sci.* **2020**, *10*, 4267. [CrossRef]
40. Shen, Y.; Liu, C.Y.; Pan, W.C.; Li, Y.J.; Wang, X.K. Design and Fully Coupled Dynamic Response Analysis of a New Floating Offshore Wind Platform. *J. Mar. Sci. Eng.* **2023**, *11*, 1368. [CrossRef]
41. Alsubal, S.; Liew, M.S.; Shawn, L.E. Preliminary Design and Dynamic Response of Multi-Purpose Floating Offshore Wind Turbine Platform: Part 1. *J. Mar. Sci. Eng.* **2022**, *10*, 336. [CrossRef]
42. *DNV-ST-N001:2023-12*; Marine Operations and Marine Warranty. DNV: Høvik, Norway, 2023.

Disclaimer/Publisher's Note: The statements, opinions and data contained in all publications are solely those of the individual author(s) and contributor(s) and not of MDPI and/or the editor(s). MDPI and/or the editor(s) disclaim responsibility for any injury to people or property resulting from any ideas, methods, instructions or products referred to in the content.